City Research Online

City, University of London Institutional Repository

This is the published version of the paper.

This version of the publication may differ from the final published version.

Non-equilibrium CFD simulation of the wet-to-dry expansion of the siloxane MM in a converging–diverging nozzle

Pawel Ogrodniczak [a,*], Martin T. White [a,b]

[a] Energy, Sustainability and Net-zero research centre (ESaAN), School of Science & Technology, City, University of London, Northampton Square, London, EC1V 0HB, UK
[b] Thermo-Fluid Mechanics Research Centre, School of Engineering and Informatics, University of Sussex, Falmer, Brighton, BN1 9RH, UK

ARTICLE INFO

ABSTRACT

Wet-to-dry organic Rankine cycles could generate 30% higher power outputs in the temperature range of 150 to 250 °C compared to existing single-phase cycles. Since the expansion is only partially wet, turboexpanders could potentially be applied provided that the wet portion of the expansion is confined to the stator to avoid erosion in the rotor. To assess the feasibility of achieving complete evaporation in the stator, two-dimensional non-equilibrium numerical simulations of the wet-to-dry expansion of siloxane MM in a covering–diverging nozzle are performed for the first time. The simulation setup is first validated against published experimental data, and a sensitivity study is conducted concerning the selected interphase models. The model is then applied to simulate expansions from inlet pressures ranging from 478 to 1250 kPa and vapour qualities from 0.1 to 0.5. Moreover, the droplet number density was varied between 10^{10} and 10^{14}. The results show that the evaporation rate, the extent of non-equilibrium effects and the flow's spatial uniformity are predominantly dependent on the droplet size. Expansions beginning with droplets smaller than 20 μm resulted in complete mixture evaporation and negligible non-equilibrium effects in almost all investigated cases. For larger droplets, ranging from 40 to 100 μm, full evaporation could only be achieved for inlet pressures above 750 kPa and inlet qualities above 0.3, whereas for lower pressures, the outlet vapour quality varied between 80 and 90%. For droplets larger than 200 μm, there is a significant delay in evaporation resulting in outlet quality typically between 40 and 70%. Larger droplet flows are characterised by substantial velocity slip, temperature difference, phase separation and lateral velocity variations. Having said this, droplet breakup analysis indicates that droplets larger than 100 μm are likely to undergo breakup, which could enhance the evaporation rate; however, this requires further investigation. In conclusion, high inlet pressures and high inlet qualities are preferred from the perspective of ensuring dry-vapour conditions at the nozzle outlet.

1. Introduction

Organic Rankine cycle (ORC) systems have been identified as a promising alternative to the conventional Rankine cycle for exploitation of low-to-medium temperature sources [1], such as renewable sources or waste heat from power plants and various industrial processes [2,3]. Despite the recent growth of the ORC market [4], achieving competitive economic performance may be hindered by several factors. ORC systems suffer from low thermal efficiencies due to low cycle temperatures, while heat transfer over small temperature differences translates to increased heat exchanger size that contributes to a higher installation cost. Furthermore, low latent heat of vapourisation, typical of organic fluids, leads to relatively high feed-pump power consumption [5]. These factors often make it challenging to achieve acceptable economic performance. In this context, cycle modifications that could increase power output without incurring additional costs could help commercialise ORC systems at a wider scale. One factor restricting further improvements in the basic ORC is the isothermal evaporation, which is responsible for a large portion of the total exergy loss [6,7]. It also limits the extent to which the heat source can be cooled due to the presence of the evaporator pinch-point, which in turn lowers the maximum attainable power output [8]. Therefore, alternative cycle architectures that could alleviate these issues have been proposed. In particular, expanding the fluid from saturated liquid or a two-phase state could fully or partially remove isothermal evaporation and consequently help achieve higher power outputs. Two-phase cycles such as the trilateral flash cycle [9–12] and partially-evaporated ORC [13–15] have demonstrated higher exergy efficiencies and power outputs when compared to single-phase cycles applied to low-temperature sources.

Nomenclature

α	Volume fraction
δ	Kronecker delta
λ	Thermal conductivity, W/m
μ	Dynamic viscosity, Pa*s
μ_t	Dynamic eddy viscosity, Pa*s
ν	Kinematic viscosity, m^2/s
ν_t	Kinematic eddy viscosity, m^2/s
ρ	Density, kg/m^3
σ	Surface tension coefficient, N/m
σ_t	Turbulent Schmidt number
τ	Stress tensor, Pa
$\mathfrak{H}$	Heat-transfer coefficient, W/m^2
A	Area, m^2
c_p	Specific heat capacity at constant pressure, J/kg*K
C_D	Drag coefficient
C_L	Lift coefficient
C_{TD}	Turbulent dispersion coefficient
D	Diameter, m
D_{LV}	Interfacial drag, N
F_D	Drag force, N
F_L	Lift force, N
Ja_T	Jakob number
M	Interphase momentum exchange
N_d	Droplet number density, $1/m^3$
Nu	Nusselt number
h	Specific enthalpy, J/kg
h_{LV}	Latent heat of vapourisation, J/kg
$\dot{m}$	Mass flow rate, kg/s
P	Pressure, Pa
Pe	Péclet number
Pr	Prandtl number
P_t	Turbulent Prandtl number
q	Vapour quality
$\dot{q}$	Heat flux, W/m^2
$\dot{Q}$	Heat transfer rate, W
Re	Reynolds number
t	Time, s
T	Temperature, K
U	Velocity, m/s

Sub- and superscripts

cr	Critical
d	Droplet
ex	Interphase exchange
in	Inlet
int	Interfacial
L	Liquid phase
mix	Mixture
out	Outlet
rel	Relative
th	Throat
V	Vapour phase
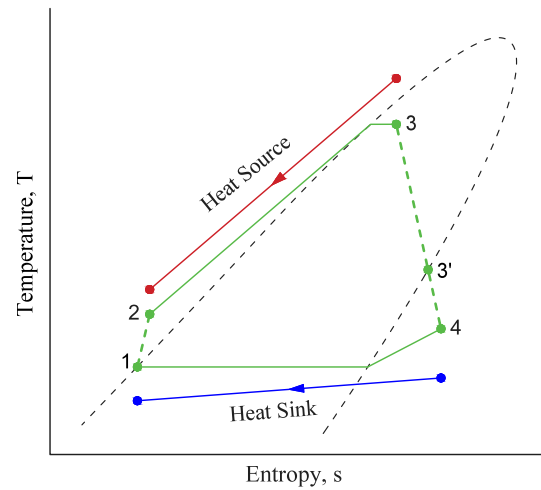
Fig. 1. Temperature-entropy diagram of the wet-to-dry cycle.

expander efficiency should be similar to that of single-phase machines. Volumetric expanders have been primarily considered since they can tolerate wet conditions. Smith et al. [16–18] performed numerical and experimental studies on two-phase expansion in screw expanders, demonstrating that efficiencies over 70% can be achieved at temperatures in the range of 100–150 °C. Murthy et al. [19] summarised the performance of various volumetric expanders and found that the efficiency of prototypes was relatively low, usually not exceeding 60%. One of the shortcomings of volumetric expanders is the limited built-in volume ratio (typically below 10) [20], which limits the application of single-stage volumetric expanders to low-temperature applications, typically below 150 °C. Impulse turbines have been proposed as alternative two-phase expansion machines. Elliott [21] carried out tests on single and two-stage axial impulse turbines for two-phase expansion of water-nitrogen mixtures and R22. A turbine efficiency of around 50% was measured, which is considerably lower than the efficiency attainable by single-phase turboexpanders. Hays and Brasz [22] employed an axial impulse turbine in their design of a turbine-compressor unit for trans-critical CO_2 refrigeration cycles. The turbine operating at 110,000 rpm could achieve an efficiency of 69%. Pelton turbines have also been considered for two-phase applications, but existing studies report low efficiencies [23,24]. An additional concern in two-phase impulse turbines is the presence of liquid droplets in the rotor, which can contribute to blade erosion, increased wear and performance deterioration. Less conventional expanders, such as rotating radial-outflow turbines and Tesla turbines have also been proposed for two-phase expansion, although numerical [25,26] and experimental [27–30] studies indicate relatively poor performance.

The review of the open literature indicates that it is challenging to design an efficient two-phase expander, especially for heat-source temperatures above 150 °C. However, within the large group of organic fluids typically applied in ORC systems, there exist fluids that have a saturation dome with a positive slope when viewed in the temperature-entropy diagram (see Fig. 1). Provided there is sufficient overhang of the saturation dome, it may be possible to operate a wet-to-dry cycle, where the fluid undergoes flash boiling and transitions from a two-phase mixture to superheated vapour under the act of depressurisation. Unlike other two-phase ORC systems, only part of the expansion occurs under the two-phase regime in the wet-to-dry cycle. This opens the possibility of employing existing turboexpander architectures, such as the radial-inflow turbine, that can achieve high volumetric expansion ratios but have previously been discarded for two-phase applications due to erosion concerns [22].

The stator plays a pivotal role in a turbine designed for the wet-to-dry cycle as it has to facilitate complete evaporation of the two-phase

Despite the potential benefits of two-phase expansion, the main challenge lies in the availability of efficient two-phase expanders. To maintain the thermodynamic advantage of two-phase expansion, the

mixture and deliver a uniform dry flow to the rotor. Elliott [21] was the first to discuss the concept of the wet-to-dry cycle. The author conducted preliminary studies, simulating the expansion of toluene from an inlet temperature of 289 °C (2.847 MPa) and quality of 0.01 to an outlet temperature of 70 °C (27.19 kPa) in a converging–diverging nozzle. The results seem promising as complete mixture evaporation was achieved maintaining a high nozzle efficiency of around 98%. The concept has been recently revisited by White [8], who performed cycle optimisation studies and preliminary radial-inflow turbine design, including numerical simulations of the two-phase expansion in the turbine stator. The author found that the wet-to-dry cycle could generate up to 30% more power than the single-phase ORC for heat source temperatures between 150 and 250 °C, using fluids such as the siloxanes MM or MDM. Ortego Sampedro and Védie [31] also conducted optimisation of the wet-to-dry cycle operating with a diphenyl-diphenyl oxide eutectic mixture. Seeking the optimum turbine inlet conditions, the authors found that two-phase inlet conditions were most favourable for heat source temperatures between 400 and 500 °C in a standalone cycle as well as a part of a cascade system. The cycle studies of White [8] were followed by three-dimensional viscous steady-state numerical simulations performed on a radial-inflow turbine stator; these indicated that the mixture could be fully evaporated. Nevertheless, the simulations were performed using a homogeneous-equilibrium model (HEM), which assumes mechanical and thermal equilibrium between the phases. In other words, the phases were forced to have identical velocities (homogeneous) and identical temperatures (equilibrium) equal to the local saturation temperature. However, the expansion through the stator involves rapid acceleration to velocities in the order of 200–300 m/s over a short distance. In such conditions, the phases may not have enough time to effectively exchange heat, while the density difference between liquid and vapour may lead to the development of velocity slip. The temperature and velocity disparity between the phases is commonly referred to as non-equilibrium effects. To investigate the significance of the non-equilibrium effects, White [32] developed a nozzle design tool based on a simplified quasi-1D two-fluid model that can generate nozzle geometries for wet-to-dry expansion, taking into account the velocity slip and thermal non-equilibrium. The author found that non-equilibrium effects can significantly affect the wet-to-dry expansion, delaying the evaporation rate, which makes the homogeneous-equilibrium model unsuitable for simulating wet-to-dry expansion. Nevertheless, the results of the quasi-1D model did indicate that it is possible to design a converging–diverging nozzle that would facilitate complete evaporation of the mixture, providing that the inlet pressure is sufficiently high. Apart from the few numerical works, Lhermet et al. [33] recently carried out an experimental study on an impulse-type axial micro turbine applied to wet-to-dry expansion of several dry fluids. Overall, it was found that as the flow entering the turbine turned from dry to wet, the turbine power output started decreasing. With an inlet quality of around 0.65, the power output dropped by 6.4% compared to the design single-phase operation. However, one should note that the turbine was nominally designed for single-phase expansion, while the vapour quality was estimated with considerable uncertainty. The experiment also did not include direct measurements of the fluid state at the stator outlet, and thus it was uncertain whether dry conditions were achieved at the stator outlet.

To date, very few works have been undertaken to validate the concept of a wet-to-dry cycle integrated with a turbomachine. Previous numerical studies either neglected the non-equilibrium effects or oversimplified the flow, assuming quasi-1D inviscid flow. This work aims to fill that gap by employing a suitable flash-boiling model to perform numerical simulations of the wet-to-dry expansion in a converging–diverging nozzle under conditions relevant to the wet-to-dry cycle, taking into account turbulence and multidimensional effects. The specific objectives and novelty of the current study are discussed in the next section, following a review of previous numerical studies of flash-boiling problems.

2. Review of numerical studies on flash-boiling problems

Flash boiling is a phenomenon that occurs when liquid is subjected to depressurisation below its boiling point, which initiates the phase-change process. Flashing is different to cavitation in that it happens at higher pressures and temperatures, and the phase-change process is assumed to be dominated by interphase heat transfer, whereas the effect of pressure non-equilibrium is deemed negligible [34,35]. Flashing is present in various technical scenarios, such as flows through cracks and restricted areas (e.g. orifices, valves) or liquid expansion through nozzles and injectors. It has been extensively studied both experimentally and numerically in the context of nuclear safety analysis [35]; specifically in the context of loss of coolant accidents [36], flow-induced instabilities in passive containment cooling systems [37], and flows through pressure relief valves [38] and nozzles [39,40]. Flashing also occurs in refrigeration systems (e.g., flashing in two-phase ejectors that replace the throttle valve) [41–43], two-phase geothermal turbines [26–28,44] and the proposed wet-to-dry cycle [8,32]. With the aim of performing a multidimensional numerical simulation of flash boiling, one first has to choose a suitable modelling technique. The most simplistic approach is to assume that both phases of the mixture have identical velocities and temperatures. Such a model is referred to as a homogeneous-equilibrium model, and as discussed, previous studies have found this assumption to be unsuitable for simulating the nozzle of a wet-to-dry turbine [32].

A slightly more advanced model, frequently employed in simulations of flash boiling, is the homogeneous-relaxation model [45]. The model also assumes identical phase velocities but accounts for a delay in evaporation by allowing the mixture quality to deviate from equilibrium. The mixture quality approaches the equilibrium quality at a rate defined by an empirically-derived time constant, and accurate results can be achieved if appropriate experimental data exist to define the relaxation time constant [41,43,46]. The major shortcoming of the homogeneous relaxation model is its lack of generality; the relaxation time constant derived for a given fluid and flow conditions may be invalid when either of these changes. For instance, Loska et al. [43] used the relaxation time expressions derived from water flash-boiling experiments to simulate flash boiling of R410a. The authors found that the mass-flow rate predictions deviated from the experimental data by 17%–25%, but once the model was tuned to the refrigerant, the deviation reduced to about 5%. Taking into account that the current study is concerned with flashing of siloxane MM, for which to the authors' best knowledge no suitable experimental measurements are available, a more general modelling approach is needed.

A more sophisticated and general technique is the two-fluid model (also referred to as the six-equation or separated model), which treats the two phases as interpenetrating continua. Separate transport equations are solved for both phases, such that each phase has its own velocity and temperature field. The two-fluid model can thus account for both velocity slip and thermal non-equilibrium. The model relies on interphase models to simulate the interaction between the phases, defined in terms of mass, momentum and energy exchange. The phase-change process is assumed to be the result of interphase heat transfer. One of the most challenging tasks when modelling flashing is the estimation of the interfacial area, which has a significant impact on the rate of interphase heat transfer. There exist nucleation models that can be used to estimate the number and size of bubbles formed in superheated liquid. Alternatively, the assumption of a constant bubble diameter, or a constant number of bubbles per unit volume, can be used as a simplified approach.

The open literature contains numerous studies based on using the two-fluid model. The majority of these have been concerned with flash boiling of sub-cooled water, where the dispersed phase is assumed to be in the form of vapour bubbles. Mimouni et al. [47] employed the two-fluid model to simulate the "Super Moby Dick" experiment [48], which involved flashing of sub-cooled water in a

converging–diverging nozzle. Nucleation models in conjunction with a constant bubble diameter were applied to estimate the interfacial area. Overall, the model proved capable of simulating flash boiling with acceptable deviations from the experimental data. The model was also applied to simulate cavitation in a flow through an orifice plate; the numerical predictions agreed with experimental observations. Marsh and O'Mahony [49] implemented the two-fluid model to simulate flash boiling of sub-cooled water in a converging–diverging nozzle referred to as the BNL nozzle. The nozzle was the subject of an experimental campaign carried out by Abuaf et al. [40]. Although there were certain discrepancies in the radial vapour distribution, the average streamwise variations were in relatively good agreement with the experimental measurements in most cases. Janet et al. [50] employed the two-fluid model to test the capability of three different wall nucleation models to predict the bubble-formation process in the BNL nozzle [40]. The authors also included the bubble coalescence effect. Provided that a suitable nucleation model was used, the model could predict average streamwise flow variations and mass flow rates relatively well. Similar to the study of Marsh and O'Mahony [49], noticeable differences were found in the radial vapour distribution, which required modification of the nucleation model used.

Liao and Lucas [51] also used the two-fluid model for simulating flashing of water in the BNL nozzle. However, in contrast to the study of Janet et al. [50], a constant bubble number, tuned to match experimental measurements, was applied. The authors found that the mass flow rate could be predicted with a maximum deviation below 7%. Overall, the model provided satisfactory estimations when average streamwise variations of pressure and vapour volume fraction are of interest, but when radial vapour distributions are concerned, much larger deviations were found, which may be due to the assumption of a constant bubble number density. In later studies [37], the authors applied the two-fluid model to simulate three flash boiling scenarios using various approaches to modelling bubble number and size. The authors simulated flash boiling in a pipe blowdown test [52], and oscillations induced by flashing in a riser pipe [36]. The constant bubble diameter and constant bubble number density assumptions were applied in those studies. The third investigation was focused on flashing in the BNL nozzle, where the authors solved a bubble number transport equation based on the nucleation models. Despite certain quantitative differences, the two-fluid model correctly predicted the trends in the first two cases. As for the BNL nozzle, the mean flow behaviour and streamwise variations well matched the experimental data, but a significant discrepancy in radial vapour phase distribution was found, similar to previous studies on the BNL nozzle. In a bid to improve the model, the authors [37] implemented the inhomogeneous multiple size group model (MUSIG) to include the effects of variable size of the vapour bubbles. The model was applied to simulate the experiment of flash boiling of water in a vertical pipe, conducted in the TOPFLOW facility dedicated to testing two-phase flows [53]. Although, the bubble size spectrum was correctly predicted, deviations in the radial vapour distribution remained, which indicates that there may have been some inaccuracy in predicting the lift and turbulent dispersion effects that affect transverse bubble migration.

Rane and He [44] employed the two-fluid model to perform a three-dimensional simulation of flash boiling of water in a curved channel of a two-phase reaction turbine designed for power generation from geothermal sources. The results showed that both the bubble number and the selected interphase heat-transfer coefficient correlation significantly affected the results. Generally, with suitable assumptions for the bubble density number and heat-transfer coefficient, the turbine power output at the design speed could be predicted within 5% of the experimental data. When the speed was lowered, the deviation increased to about 30%–50%. On the other hand, the predicted mass flow rate was accurate within the whole operation range. The average variation of vapour mass fraction was also captured relatively well, with the model slightly underestimating the vapour generation rate.

Nevertheless, the trends were well conserved. The authors later employed the model to study flash boiling in a modified turbine geometry, including a rotor-stator assembly [26].

In all these cited studies, the dispersed phase was assumed to be vapour, although in some cases the void fraction at the outlet exceeded 0.7, which could mean this assumption is no longer valid. This was recognised by Ortego Sampedro et al. [54], who proposed a transitional model, based on the two-fluid model, that is capable of switching from the bubbly to droplet flow regime. This model was found to be more flexible than other existing models as it could be well calibrated using the droplet and bubble numbers, and predict simultaneously the mass flow rate and nozzle efficiency.

In summary, the two-fluid model has been successfully applied to simulate various flash boiling problems. It has been found to be capable of providing relatively accurate estimates of the overall flow behaviour and the phase-change process when applied to in-nozzle flashing, which is directly relevant to the current study. In the current study, the two-fluid model has been employed for the first time to perform a two-dimensional viscous non-equilibrium CFD simulation of the wet-to-dry expansion of siloxane MM in a planar converging–diverging nozzle. Although, the two-fluid model has been previously applied to study wet-to-dry expansion [32], the analysis was simplified to quasi-1D flow, and only gave insight into average flow variations, while neglecting the effects of turbulence and spatial variations. In contrast to previous CFD studies, flashing from a two-phase state does not involve the nucleation process, and hence nucleation models cannot be applied to estimate the interfacial area. Moreover, adjustments are necessary since the liquid is now the dispersed phase, while the vapour phase cannot be fixed to saturation conditions (a common assumption in previous studies) to allow the transition to superheated conditions. In the following sections, a description of the model is provided including a validation study against experimental data for flash boiling of water. Following this, sensitivity studies are performed concerning the selected interphase models. The model is then applied to study the wet-to-dry expansion of the siloxane MM under operating conditions relevant to the wet-to-dry cycle. The results of the simulations give insight into the expansion characteristics for inlet pressure ranging from 478 kPa to 1250 kPa, inlet quality from 0.1 to 0.5 and droplet numbers ranging from 10^{10} to 10^{14} droplets per unit volume. The results reveal the degree of flow non-uniformity in terms of two-dimensional variations of flow properties within the nozzle. Furthermore, droplet breakup analysis is conducted to investigate the effects of possible droplet breakup and assess the realistic size of droplets throughout the expansion. This work further assesses the feasibility of constructing a nozzle for the wet-to-dry cycle that could facilitate complete evaporation of the mixture.

3. Two-fluid model

This section provides an overview of the two-fluid model applied to flash-boiling flows. It is important to note that this section only outlines general concepts and modelling techniques, while a detailed description of the model, including the flow governing equations, is provided in Appendix A.

3.1. Overview

In the two-fluid model, the Eulerian-Eulerian framework is employed, which means that both phases are treated as interpenetrating continua. The conservation of mass, momentum and energy equations are formulated similarly to single-phase flows with the difference that in two-phase problems, there can be two phases in each control volume, and the phases interact by exchanging mass, momentum and energy. Hence, each term in the governing equations is multiplied by the volume fraction of the corresponding phase to account for a fraction of the control volume that the given phase occupies (see Appendix A.1 for details). The interaction between the phases is taken into account

by including source/sink terms that are evaluated through interphase models. The critical parameter influencing the phases' interaction is the interfacial area. Due to liquid density being substantially higher than that of vapour, even the expansions from low vapour quality are likely to be in the form of droplet flows. Hence, the interfacial area in the current investigation is simply the combined surface area of all the droplets. Since the expansion begins in the two-phase state, the nucleation models cannot be applied to estimate the number and size of droplets. Nonetheless, two alternative approaches can be followed, namely, a constant droplet size or a fixed number of droplets per unit volume (droplet number density). The latter technique was applied in this work because it can better reflect the physical process of boiling as the droplets are allowed to change size [55]. Assuming there are N_d droplets per unit volume, the interfacial area per unit volume A_{int} can be defined as:

$$A_{int} = N_d\, \pi D_d^2 = 6\frac{\alpha_L}{D_d} \tag{1}$$

where α_L is liquid volume fraction and D_d is the droplet diameter.

3.2. Phase change — mass and heat transfer

A common assumption made when simulating flashing is that phase change happens solely due to interphase heat transfer; this assumption was also followed in this study. The interphase mass and heat transfer are therefore closely linked. The heat transfer was modelled using a two-resistance model, which assumes an interface between the continuous and dispersed phases, which is at local thermodynamic equilibrium conditions (i.e., saturation conditions). The heat transfer occurs between the phases and the interface separately. An energy balance can be applied across the interface to determine the mass transfer (vapourisation rate):

$$\dot{m}_{ex} = \frac{\dot{q}_L + \dot{q}_V}{h_V - h_L} = \frac{\mathfrak{H}_L A_{int}\left(T_{int} - T_L\right) + \mathfrak{H}_V A_{int}\left(T_{int} - T_V\right)}{h_V - h_L} \tag{2}$$

where $\dot{m}_{ex}$ is the interphase mass transfer, $\dot{q}_L$ and $\dot{q}_V$ represent heat exchanged between the liquid and the interface, and between the vapour and the interface respectively; h_L and h_V are liquid and vapour specific enthalpies, A_{int} is the interfacial area, while T_L, T_V and T_{int} are the interface, liquid and vapour temperatures respectively. One can notice that the vapourisation rate also depends on the liquid and vapour heat-transfer coefficients $\mathfrak{H}_L$ and $\mathfrak{H}_V$; these are estimated using the interphase models. In this work, $\mathfrak{H}_V$ was evaluated with the Ranz-Marshall [56] correlation, which was derived from experimental tests on a water droplet evaporating in a hot air stream. For the heat-transfer coefficient on the liquid side, one can presume a constant Nusselt number of 6, which is an approximation derived from a transient heat-transfer analysis applied to a solid sphere [57].

3.3. Momentum transfer

The interphase momentum exchange in a droplet flow can be broken down into three major mechanisms: drag, lift and turbulent dispersion forces. The drag develops due to a difference in phases density; the drag coefficient was evaluated by means of the Ishii-Zuber [58] model, which is capable of accounting for shape distortion and the effect of densely distributed particles, making it suitable for flows with both dilute and densely distributed droplets. The lift force drives the droplets' lateral migration; the lift coefficient was evaluated using the Tomiyama [59] model, which can also account for shape distortion effects. Turbulence enhances the distribution of the dispersed phase from regions of high concentration to regions of low concentration of the dispersed phase. Favre Averaged Drag was used for estimating the turbulent dispersion, which proved suitable for a wide range of applications [57].

3.4. Comment on the interphase models

In summary, the interphase models are employed to estimate vapour and liquid heat-transfer coefficients, as well as, the drag, lift and turbulent dispersion effects. The details of each of these models can be found in Appendix A.2. The interphase models constitute the critical part of the two-fluid model; arguably, the two-fluid model can be less reliable than the simplified models if unsuitable models are used [34]. Recognising the importance of the interphase models, the authors decided to first assess the sensitivity of the solution to the type of interphase models used and to confirm the reliability of the current setup. The results of the sensitivity studies are presented in Section 4.5.

3.5. Numerical implementation

The two-fluid model described above was implemented in ANSYS CFX 2021 R1 [60], which uses a finite-volume approach to solve Reynolds-Averaged Navier Stokes (RANS) equations. Steady-state analysis was selected with high-resolution discretisation schemes applied to advection terms. The turbulence in the continuous phase is modelled with the $k - \omega$ SST model. A dispersed phase zero equation model is applied to evaluate the eddy viscosity of the dispersed phase [61]; the details of the dispersed phase zero equation model are included in Appendix A.3. An automatic wall function was applied to resolve gradients in the boundary layer zone. The automatic wall function approach can switch from directly resolving the boundary layer to applying wall functions, depending on the local y^+ value. Since the current work is concerned with studying organic fluids, which tend to considerably deviate from the ideal-gas law, a suitable equation of state is needed to accurately predict fluid's thermodynamic properties. The model employs NIST REFPROP 10.0 [62], which uses the Helmholtz-energy based equation of state that has been derived specifically for siloxane MM, using empirical and molecular simulation data [63]. Fluid properties were introduced in the form of look-up tables which were constructed for a number of pressure-temperature pairs within specified pressure and temperature intervals. The liquid and vapour properties were extended into the metastable region and calculated up until the spinodal limit so that the solver could evaluate phase properties in the metastable regime (i.e. when the liquid becomes superheated or vapour becomes subcooled).

3.6. Two-fluid model validation

The purpose of the validation is two-fold; to test whether the model has been set up correctly and to validate the in-house tool that is used to construct look-up tables that extend into the metastable region. For this purpose, the converging–diverging nozzle studied experimentally by Abuaf et al. [40], referred to as the BNL nozzle, was selected. In these experiments, water was expanded from the subcooled liquid state, which means that the assumption of the dispersed phase in the form of spherical liquid droplets is not valid (at least in the early stage of expansion). Expansion from a low-quality mixture, rather than a subcooled liquid state, would be more relevant to the present study; however, such experimental data is currently unavailable. It is thus necessary to modify the model described earlier to work with vapour as the dispersed phase. It is presumed that if a modified version of the model (suited to a dispersed vapour phase) is validated, its applicability to droplet flows will also be established. Another benefit of using the BNL tests as validation is the possibility of comparing the results to other existing numerical studies [44,51]. The main difference between these previous studies is the use of look-up tables generated by REFPROP 10.0 [62]. The details concerning the BNL nozzle geometry, the required setup adjustments and the mesh independence study can be found in Appendix B.

Table 1 illustrates the comparison of the average water mass flow rate at the nozzle outlet with previous studies. It is evident that the average mass flow rate is very close to the values obtained by Rane & He,
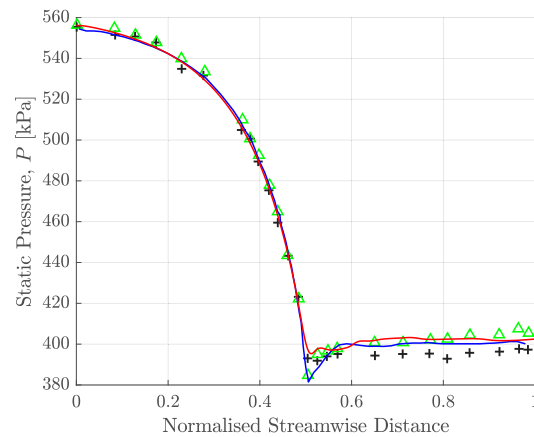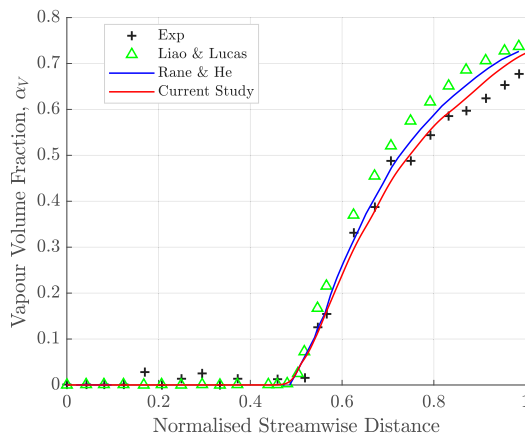
Fig. 2. The variation of static pressure and vapour volume fraction along the centre line of the BNL nozzle; comparison between the current study, other numerical studies and the experimental measurements.

and Liao & Lucas, with a similar discrepancy of about 4.9%, compared to the experimental data. Although the solution for the BNL nozzle exhibited certain small fluctuations, the fluctuations were sufficiently small to be ignored when comparing instantaneous values to the results of the other studies and the experimental measurements. Fig. 2 presents the comparison of the centre-line distribution of pressure and vapour volume fraction. It is evident that the overall trends and values closely resemble the other numerical studies and the experimental results, which confirms the validity of the developed model coupled with the look-up tables.

4. Simulation of the wet-to-dry expansion of the siloxane MM

The validated two-fluid model is now applied to study the wet-to-dry expansion of siloxane MM; a fluid identified as one of the best candidates for the wet-to-dry cycle [8]. For this purpose, a simple planar converging–diverging nozzle was created. A range of inlet conditions defined in terms of inlet pressure and vapour quality were simulated to assess the feasibility of the wet-to-dry nozzle design under various operating conditions. Different droplet numbers were also simulated to examine how the solution may vary with the droplet size.

4.1. Wet-to-dry nozzle design

The main objective of this work is to perform numerical analysis to assess the overall characteristics of wet-to-dry expansion, taking into account the non-equilibrium effects. As the goal is not to generate an optimal geometry, the most straightforward two-phase nozzle design approach was followed, based on the assumption of quasi-1D isentropic two-phase flow in mechanical and thermal equilibrium (homogeneous-equilibrium model). The flow is assumed to be quasi-1D in the sense that all the flow properties vary only along the longitudinal axis of the nozzle x. Apart from these assumptions, the ratio of nozzle width to the throat height b/o_{th}, and the ratio of the nozzle length to its throat L_N/o_{th} are defined. Appropriate boundary conditions are selected to ensure the fluid can transition from a two-phase state to a superheated vapour. The boundary conditions are defined by the inlet pressure P_{in} and inlet quality q_{in}, alongside the mass flow rate $\dot{m}$ and inlet velocity u_{in}. Nozzle outlet conditions are selected to correspond to the expected stator outlet pressure within a practical wet-to-dry cycle. The cycle condensation temperature T_{cond} and the turbine degree of reaction R determine the nozzle outlet conditions. The degree of reaction is particularly important in the design of a turbine for the wet-to-dry cycle as it determines the fraction of the total expansion that happens in the stator. Hence, this has to be sufficiently high to ensure that the fluid can escape the two-phase dome (see Fig. 4). With the boundary conditions defined, the nozzle pressure profile is defined using a Bezier
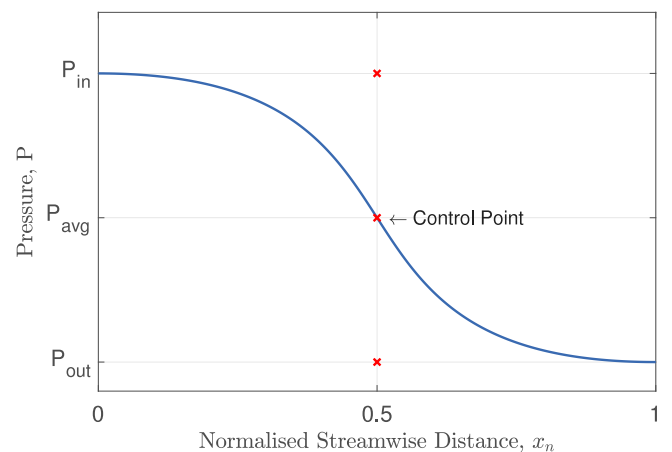
Fig. 3. The imposed pressure profile constructed using a Bezier curve with three control points.

Table 1
Comparison of average mass outflow with other numerical studies and experimental data for the BNL nozzle.

	Current model	Experimental [40]	Liao & Lucas [51]	Rane & He [44]
Mass flow rate [kg/s]	8.37	8.80	8.40	8.38
Difference [%]	–	4.89	0.36	0.12

curve with three control points. The Bezier control points are positioned such that the pressure gradient approaches zero at the inlet and outlet of the nozzle. Moreover, the pressure at the middle of the nozzle is set to the average of the inlet and outlet pressures. The imposed pressure profile is identical in each investigated case and has been illustrated in Fig. 3. Once the pressure profile has been defined, all other fluid properties are obtained using pressure-entropy data, while flow velocity and nozzle cross-sectional area can be derived from the conservation laws. As noted, the nozzle geometries generated using this approach are considered suitable for generating baseline geometries that enable investigations into wet-to-dry expansion. Whilst, the use of a non-equilibrium design tool, alongside the optimisation of the pressure profile, could be expected to lead to more optimal designs, such an investigation is left for subsequent studies.
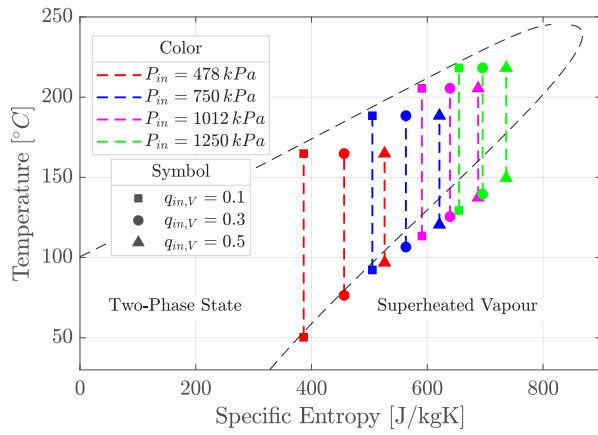
Fig. 4. The temperature–entropy diagram of the twelve simulated expansion cases; the depicted expansions define the boundary conditions used in the nozzle design and CFD simulations, and are generated under the assumption of isentropic homogeneous-equilibrium flow.

Table 2
Geometrical features of each investigated converging–diverging nozzle.

P_{in} [kPa]	$\dot{q}_{V,in}$	P_{out} [kPa]	H_{in} [mm]	o_{th} [mm]	H_{out} [mm]	L_{th} [mm]	L_N [mm]	Grid size [elements]
478	0.10	15.14	13.50	7.25	83.90	78.58	217.62	67,480
478	0.30	40.95	27.10	7.92	34.26	98.83	237.49	59,186
478	0.50	63.51	39.78	8.40	22.63	111.60	252.04	60,005
750	0.10	63.51	11.90	6.05	30.40	66.68	181.41	39,234
750	0.30	72.96	21.63	6.50	24.67	80.08	194.88	41,892
750	0.50	79.79	30.81	6.84	21.47	88.42	205.12	44,360
1012	0.10	77.37	11.28	5.37	27.61	59.18	161.02	33,071
1012	0.30	85.83	18.63	5.70	23.53	69.08	170.87	34,763
1012	0.50	92.06	25.64	5.95	21.07	75.47	178.63	36,546
1250	0.10	88.28	11.11	4.94	26.05	54.94	148.20	29,348
1250	0.30	95.72	16.81	5.19	22.98	62.08	155.68	30,680
1250	0.50	101.30	22.29	5.39	20.99	67.33	161.79	32,008

4.2. Investigated operating conditions

The boundary conditions were selected to ensure the fluid can transition from the two-phase state to a superheated vapour under the isentropic homogeneous-equilibrium flow assumption. To provide a thorough assessment of the performance of the wet-to-dry nozzle under different working conditions, twelve expansion cases were considered, similar to the ones considered by White [32]. The twelve expansion cases were defined in terms of inlet pressure and vapour quality; four inlet pressures were tested, 478, 750, 1012 and 1250 kPa, and three inlet qualities, 0.1, 0.3 and 0.5. Cycle condensation temperature T_{cond} was fixed at 40 °C, while the degree of reaction R was set to 0.5 for all the operating points except for the expansion from 478 kPa, for which R had to be lowered to 0.1 and 0.4 for inlet qualities of 0.1 and 0.3 respectively, to ensure the fluid transitions into the superheated vapour region. The twelve expansion cases are illustrated in Fig. 4. In order to generate a nozzle geometry for each of the investigated expansion cases, the remaining boundary conditions and design assumptions were defined as follows: inlet velocity u_{in} and mass flow rate $\dot{m}$ were set to 10 m/s and 0.5 kg/s, whereas the geometrical ratios b/o_{th} and L/o_{th} were set to 3 and 30 respectively. Fig. 5 presents a nozzle geometry for one of the investigated operating points, alongside the numerical mesh. Using the same notation defined in Fig. 5, Table 2 provides the dimensions of all the examined geometries alongside the grid size. Although the mass flow rate was chosen somewhat arbitrarily, the simulations were also performed for mass flow rates of 0.05 and 5 kg/s and no significant changes were found in the phase-change process. Hence, scale effects are deemed to be of secondary importance.

Table 3
Mesh independence study for the wet-to-dry expansion from $P_{in} = 1012$ kPa and $q_{V,in} = 0.3$.

Element count [×10³]	$\dot{m}_{out}$ [g/s]	$u_{V,out}$ [m/s]	$u_{L,out}$ [m/s]	$T_{V,out}$ [K]	$T_{L,out}$ [K]	$q_{V,out}$
15	5.057	266.62	250.47	403.57	375.58	0.9843
23	5.064	266.47	249.71	403.53	375.92	0.9839
35	5.065	266.46	249.38	403.52	376.12	0.9838
52	5.062	266.52	249.27	403.53	376.24	0.9838

4.3. Numerical setup

Generally, the numerical setup is identical to the one described in Section 3. As CFX cannot carry out 2D simulations, a thin slab of the nozzle 0.15 mm thick was considered and the mesh was extruded by a single element in the spanwise direction. Symmetry boundary conditions on the upper and lower faces of the slab are then applied. For the look-up tables, a pressure range between 1 and 1800 kPa, and a temperature range between −23 °C and 277 °C were considered, which are divided into 500 distinct points such that a 500 × 500 table resolution was obtained. A constant droplet number density N_d is assumed to estimate droplet size and distribution. The droplet density number is one of the main unknowns in the simulation. In the absence of experimental data, it is difficult to state what value for N_d would be appropriate. Therefore, the subsequent analysis will examine a range of N_d values, ranging from 10^{10} to 10^{14} droplets per unit volume. The higher limit of $N_d = 10^{14}$ was chosen as at this droplet number the solution begins to resemble homogeneous-equilibrium flow; this indicated that the droplets were sufficiently small for the non-equilibrium effects to be negligible. On the other hand, the lower limit $N_d = 10^{10}$ was selected based on a Weber-number analysis; below $N_d = 10^{10}$ the droplets become so large that breakup is very likely to happen at the beginning of the expansion leading to an eventual increase in N_d. Further details about the droplet breakup model can be found in Section 6. It is worth noting that for each case, the homogeneous-equilibrium solution is first obtained, which was then used to initialise a homogeneous flow in thermal non-equilibrium. Finally, the solution of the homogeneous non-equilibrium simulation was used to initialise the two-fluid simulation accounting for both velocity and temperature non-equilibrium effects. Without the multi-step initialisation procedure, the full non-equilibrium simulation struggled to converge, although the authors found that starting with a very coarse mesh could also help achieve convergence without employing the simplified models.

4.4. Mesh independence study

One particular expansion case, with P_{in} of 1012 kPa and $q_{V,in}$ of 0.3, was selected to perform a mesh independence study to determine the suitable mesh element size that will be applied to the rest of the investigated cases. The mesh was predominantly a structured mesh with hexahedral elements, as shown in Fig. 5. A single element was applied in the spanwise direction to perform a quasi-2D simulation. The mesh was resolved near the walls, with a target y^+ between 30 and 200 for both phases. The solution converged well, with mass and momentum residuals below 10^{-6}, while the average flow parameters at the outlet (e.g. mass flow rate, velocity etc.) converged to near single values.

Table 3 shows how the total mass flow rate and mass flow-averaged flow properties at the nozzle outlet vary with the mesh element size. Generally, it can be observed that the variations are extremely small and become virtually negligible when the number of elements was increased above 35×10^3. The extremely small variations can be attributed to a relatively small element size that the mesh study began with, and a near-wall refinement that was kept constant for each grid. Apart from the variation in outlet properties, radial profiles of pressure
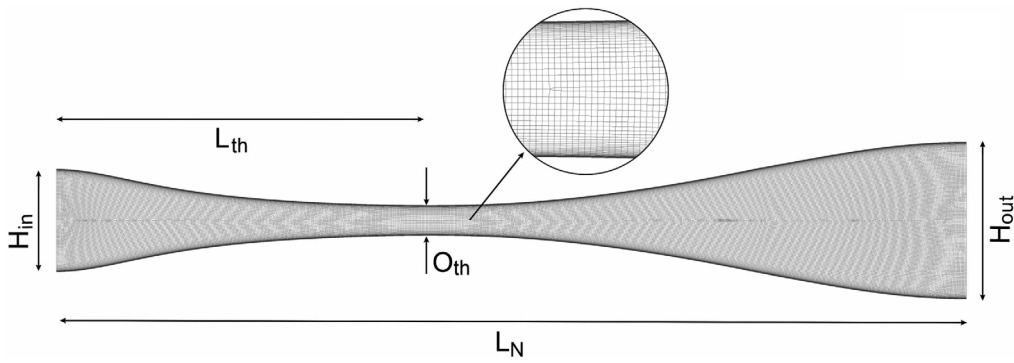
Fig. 5. Nozzle geometry for the expansion from 478 kPa and inlet quality of 0.3; the figure also illustrates the type of mesh used in the simulations — similar mesh was constructed for all other geometries.
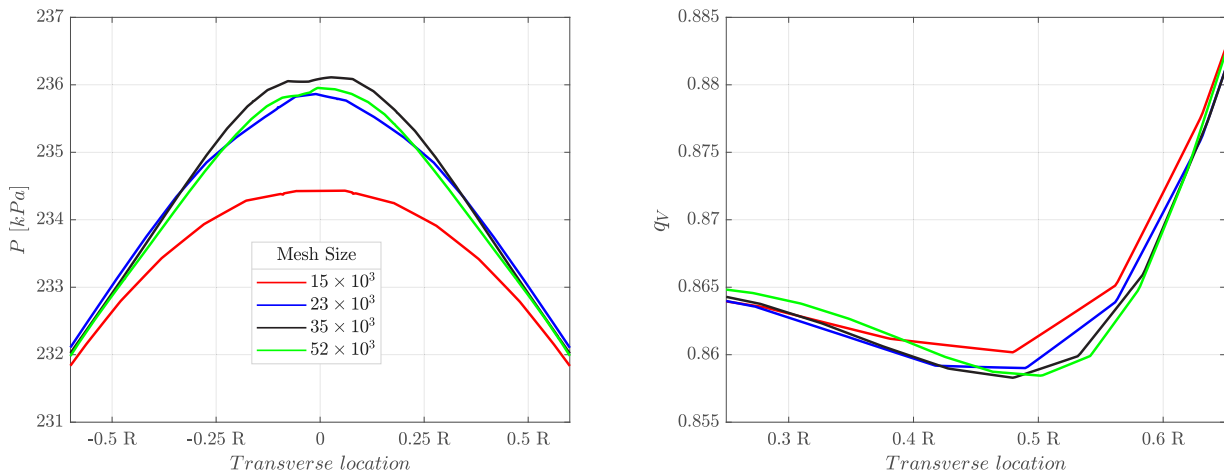
Fig. 6. Dependence of transverse profiles of static pressure P and vapour quality q_V on the mesh resolution; the profiles were taken approximately midway between the throat and the outlet and were capped to illustrate only the regions where the parameters were sensitive to mesh resolution.

and vapour quality are compared in Fig. 6. The profiles were taken at a plane halfway between the nozzle throat and the outlet and only the portion of the profiles where a visible dependency on mesh resolution was present is shown. It is found that the radial profiles practically overlap when the number of elements was increased above 23×10^3. Even for the coarsest mesh with 15×10^3 elements, the maximum difference in pressure was below 0.7%, while the difference in the vapour quality was even smaller. Radial profiles of other parameters, as well as average streamwise variation were also checked, but negligible differences between consecutive meshes were found. Based on the mesh independence study results presented above, the grid with 23×10^3 elements could be readily considered sufficiently fine. However, to ensure the mesh is suitable for all other investigated the element size corresponding to 35×10^3 elements grid was applied to mesh all other nozzle geometries (the element size corresponding to 35×10^3 elements was 0.36 mm).

4.5. Sensitivity to interphase models

Before proceeding with the parametric study, the sensitivity of the solution to interphase models is assessed to gain extra confidence in the model. Two alternative drag models were tested, namely, Grace [64] and Shiller-Naumann [65] models. The Grace model has been derived for a flow past a single bubble based on the air–water flows and can account for particle shape distortion, while the latter was derived for a flow past a solid particle, and does not take into account shape distortion effects. Although the alternative drag models have slightly different formulations it is presumed that if the model is reliable, the other models should not generate drastically different results, with

overall trends conserved. Other momentum exchange models, including the lift force and turbulent dispersion effects, are thought to be of secondary importance (at least when average streamwise variations are of interest) and have been neglected in the sensitivity study.

Fig. 7 presents the streamwise profiles of average vapour quality $\bar{q}_V$ and mixture velocity $\bar{u}_{mix}$ obtained with the two alternative drag models and the baseline model. Two expansion cases were simulated: the expansion from 478 kPa and inlet quality of 0.3, and the expansion from 1012 kPa and the same inlet quality. The mixture velocity is defined as the mass-fraction weighted sum of liquid and vapour velocities (i.e., $u_{mix} = q_V u_V + q_L u_L$). For $N_d = 10^{14}$, the solution is practically independent of the type of drag model used. This is because the flow closely resembles homogeneous-equilibrium flow with negligible velocity slip. For lower droplet numbers, very small discrepancies were noticed. A slightly lower vapour generation rate was estimated when the Schiller-Naumann model was employed for the expansion from 478 kPa with N_d fixed at 10^{10}, predicting approximately 5% lower outlet quality than the baseline model. The Grace model slightly deviated from the baseline prediction in the converging section of the nozzle; however, the results of the two models merge in the diverging section. Overall, the type of the drag model was found to have very limited influence on the expansion.

When it comes to the models for predicting the heat-transfer rate on the continuous side of the interface there are generally two main families of correlations [44]. The first family is based on the dispersed particle Reynolds number Re_d (Eq. (21)) and continuous phase Prandtl number Pr_V (Eq. (22)), while the other is based on Péclet and Jakob numbers. Péclet number is simply the product of Re_D and Pr_V, while the Jakob number represents the ratio of the heat required to bring
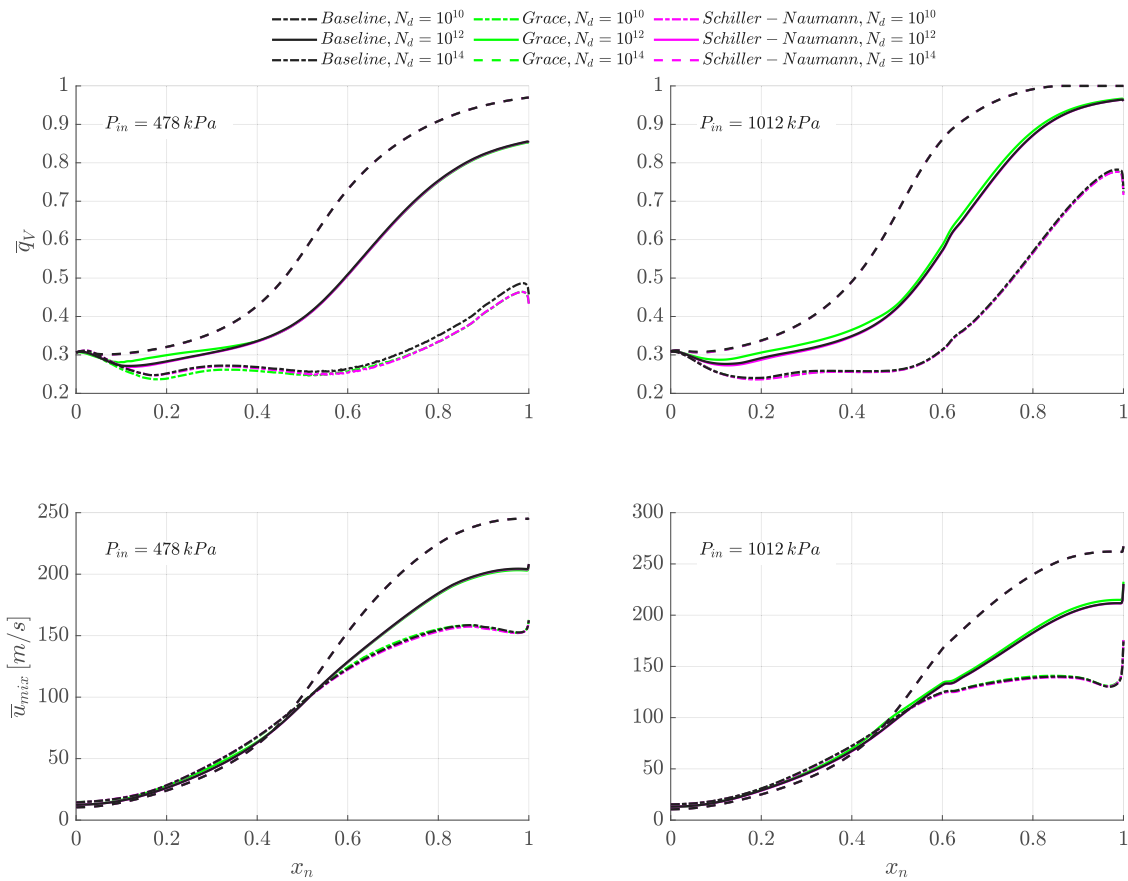
Fig. 7. Streamwise variation of average vapour mass fraction $\overline{q}_V$ and average mixture velocity $\overline{u}_{mix}$ obtained using alternative interphase drag models. The plot shows two expansion cases: the expansion from 478 and 1012 kPa with inlet quality of 0.3.

the continuous phase to the saturation conditions to the latent heat of the corresponding volume of the dispersed phase. In this sensitivity study, one correlation representing each family will be tested, namely, the Ranz-Marshall [56] correlation, and the Wolfert [66] correlation expressed as:

$$Nu_V = \frac{12 Ja_T}{\pi} + 2\sqrt{\frac{Pe}{\pi}} \qquad (3)$$

For the heat-transfer coefficient between the droplet and the interface, a Nusselt number of 6 was initially assumed, which is an approximation based on the transient heat-transfer analysis in a solid sphere. To investigate the sensitivity of the solution to the heat-transfer rate on the droplet side, two different values of Nu_L were simulated, namely $Nu_L = 2$ and $Nu_L = 12$, corresponding to reduced and enhanced heat-transfer rates in relation to the original assumption.

Fig. 8 shows the comparison between $\overline{q}_V$ and $\overline{u}_{mix}$ for the various heat-transfer coefficient formulations. The same expansion cases were selected as in the study of sensitivity to interphase drag models (see Fig. 7). It was found that the type of heat-transfer rate formulation had a higher impact on the solution than the drag model. Generally, the Wolfert model tends to predict slightly enhanced evaporation rates, with outlet quality up to 5% higher than the baseline prediction. Enhanced evaporation rate also translates to higher mixture velocities but the difference is also small, within 3% percent. As expected, raising Nu_L to 12 enhanced the evaporation rate, with the maximum difference in the streamwise vapour quality profile reaching about 10%. Quicker evaporation was also associated with higher overall velocities, but the maximum difference was about 6%. Lowering Nu_L to 2 visibly reduced the evaporation rate, resulting in considerably smaller vapour quality throughout the expansion. The maximum difference in q_V was

below 14% when compared to the baseline streamwise variation. Something peculiar can be noticed in that for a droplet number of 10^{12} the mixture eventually reaches outlet quality similar to the one predicted by the baseline model, despite a smaller Nu_L. One possible explanation is that a reduced Nu_L causes the droplets to develop a higher superheat level, which in turn accelerates the heat transfer (see Eq. (4)). Although the outlet quality may be similar to the baseline model, there is still a visible reduction in the mixture velocity. This is because throughout much of the expansion, the quality was lower and droplets were larger. Larger droplets in turn experience higher drag effects contributing to increased interphase friction, energy loss and consequently lower outlet velocities. The maximum deviation of the mixture velocity profile for $Nu_L = 2$ reached about 12%.

Summarising the sensitivity study, it was found that the solution is much more sensitive to the interphase heat transfer models than to interphase drag models. Moreover, the sensitivity to the heat transfer model applied on the vapour side was small, while the solution changed more significantly when the liquid side Nusselt number was changed. This was expected as this directly influences the droplet evaporation rate. Although the quantitative changes were moderately high (below 15%), the qualitative trends were conserved across all cases. The sensitivity study, therefore, showed that the model can be successfully used for preliminary analysis and can be useful when evaluating the feasibility of a two-phase nozzle for the wet-to-dry cycle. However, one should remember that certain assumptions, such as the value of the Nusselt number, carry certain uncertainty as shown in this sensitivity analysis.

5. Parametric study results

This section presents the results of the numerical simulations performed for the twelve expansion cases depicted in Fig. 4. The influence
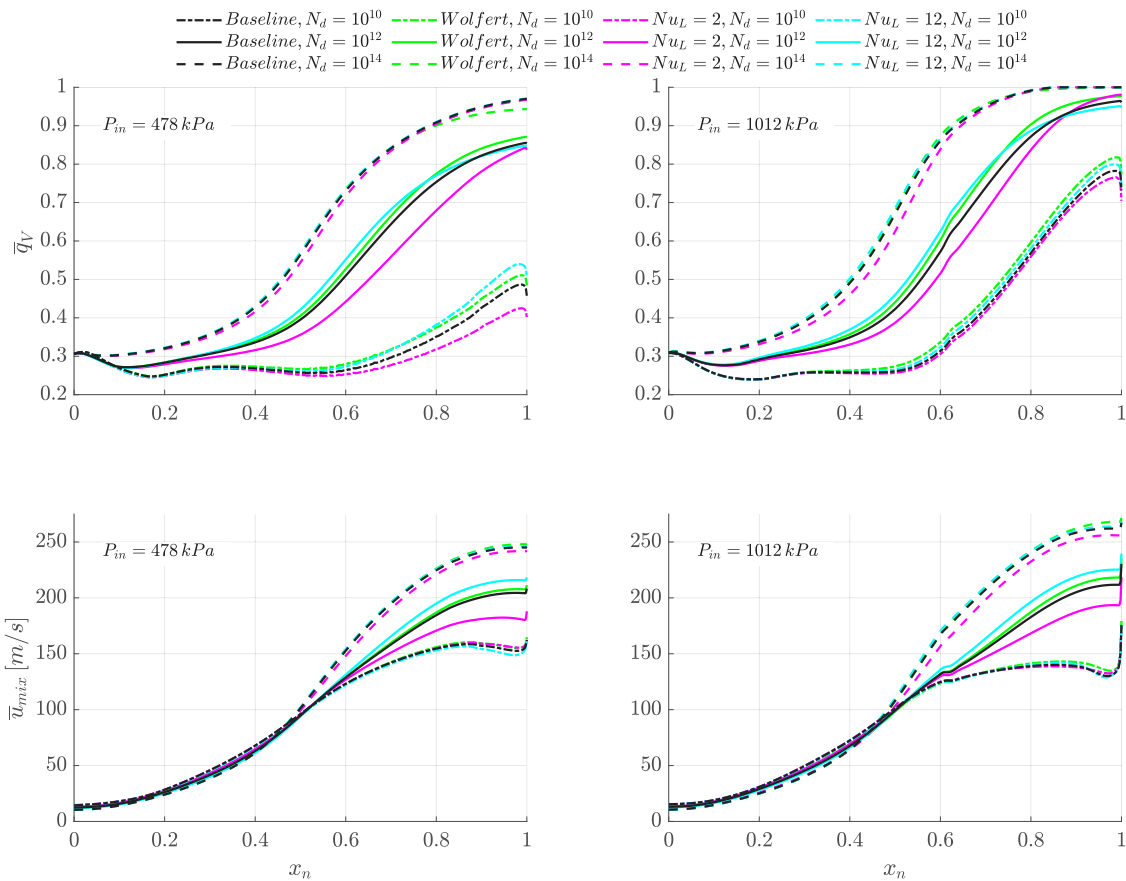
Fig. 8. Streamwise variation of average vapour mass fraction $\bar{q}_V$ and average mixture velocity $\bar{u}_{mix}$ obtained using alternative heat-transfer coefficient models. The plot shows two expansion cases: the expansion from 478 and 1012 kPa with an inlet quality of 0.3.

of inlet conditions and droplet number on the evaporation rate and the development of non-equilibrium effects is discussed. The results also give insight into the uniformity of the flow in different expansion conditions. To understand the following discussion, one should remember that higher droplet numbers are equivalent to a higher number of smaller droplets, whilst lower droplet numbers represent fewer larger droplets for a given volume fraction of liquid. Hence, the terms "high droplet number" and "small droplets" or "low droplet numbers" and "large droplets" can be used interchangeably.

5.1. Mixture evaporation

All the expansion cases were designed under the assumption of a homogeneous-equilibrium flow, which predicted full vapourisation in each case. Therefore, the first comparison aims to investigate whether vaporisation can be achieved when non-equilibrium effects are considered. Fig. 9 illustrates the streamwise variation of average vapour mass fraction $\bar{q}_V$ for all the investigated boundary conditions and droplet numbers. The normalised streamwise distance was denoted by x_n. The plot presents the predicted evolution of q_V assuming three different droplet numbers, namely 10^{10}, 10^{12} and 10^{14}. For the expansion from the highest pressure of 1250 kPa, the simulation did not converge when N_d was set to 10^{10}. This happened because of excessive liquid superheating, which essentially led to liquid pressure falling below the spinodal pressure; a similar issue was encountered by White [32]. In simple terms, liquid MM became superheated to an extent that the equation of state could not reliably estimate the fluid properties, which in consequence led to solution divergence.

Analysing Fig. 9 it is clear that N_d has a significant impact on the evaporation rate. If $N_d \geq 10^{14}$, one can expect complete evaporation of the two-phase mixture for any inlet quality above 10%, provided

that the inlet pressure is above 1012 kPa. Reducing P_{in} to 750 kPa and maintaining $N_d = 10^{14}$, complete evaporation occurs for $q_{V,in} \geq 0.3$, whereas for $q_{V,in} = 0.1$ the fluid leaving the nozzle has a small liquid content, typically about 3% by mass. Bringing the inlet pressure down to 478 kPa, while maintaining $N_d = 10^{14}$, full transition to dry vapour is only predicted to happen for expansion from $q_{V,in} \geq 0.5$. For lower inlet quality, a small amount of liquid may be present at the nozzle outlet. The situation changes drastically when the droplet number is reduced. For $N_d = 10^{12}$, dry outlet conditions were achieved only for the expansion from P_{in} of 1250 kPa and $q_{in} \geq 0.3$. For P_{in} at 1012 kPa, near-dry conditions were achieved for $q_{in} \geq 0.3$. For lower pressures, the mixture did not manage to fully evaporate. Lowering N_d to 10^{10} resulted in a further decrease of the evaporation rate; for the lower-pressure expansions (for P_{in} at 478 and 750 kPa) the mixture was not even close to dry conditions, having a significant amount of liquid present at the outlet for all of the investigated inlet vapour qualities. For the expansion from 1012 kPa, only in case of sufficiently high inlet quality of 0.5 or higher, the fluid is expected to transition to a superheated vapour; expansion from lower $q_{V,in}$ was associated with a considerable amount of liquid at the outlet.

Referring to the droplet number, one may find it difficult to visualise what sort of droplet size each simulated case with a fixed droplet number corresponds to. Fig. 10 illustrates the relationship between inlet droplet diameter $D_{d,in}$ and outlet vapour quality $q_{V,out}$ for all the investigated cases. Although the plot does not distinguish between different inlet qualities, knowing that for a given P_{in}–N_d pair, higher inlet vapour qualities are characterised by smaller initial droplets, it can be readily deduced which data corresponds to individual inlet qualities. First, it can be noted that the initial droplet size range corresponding to $N_d = 10^{10}$ is around 200–450 μm. Having $D_{d,in}$ in that size range results in partial evaporation of the mixture with a relatively high liquid
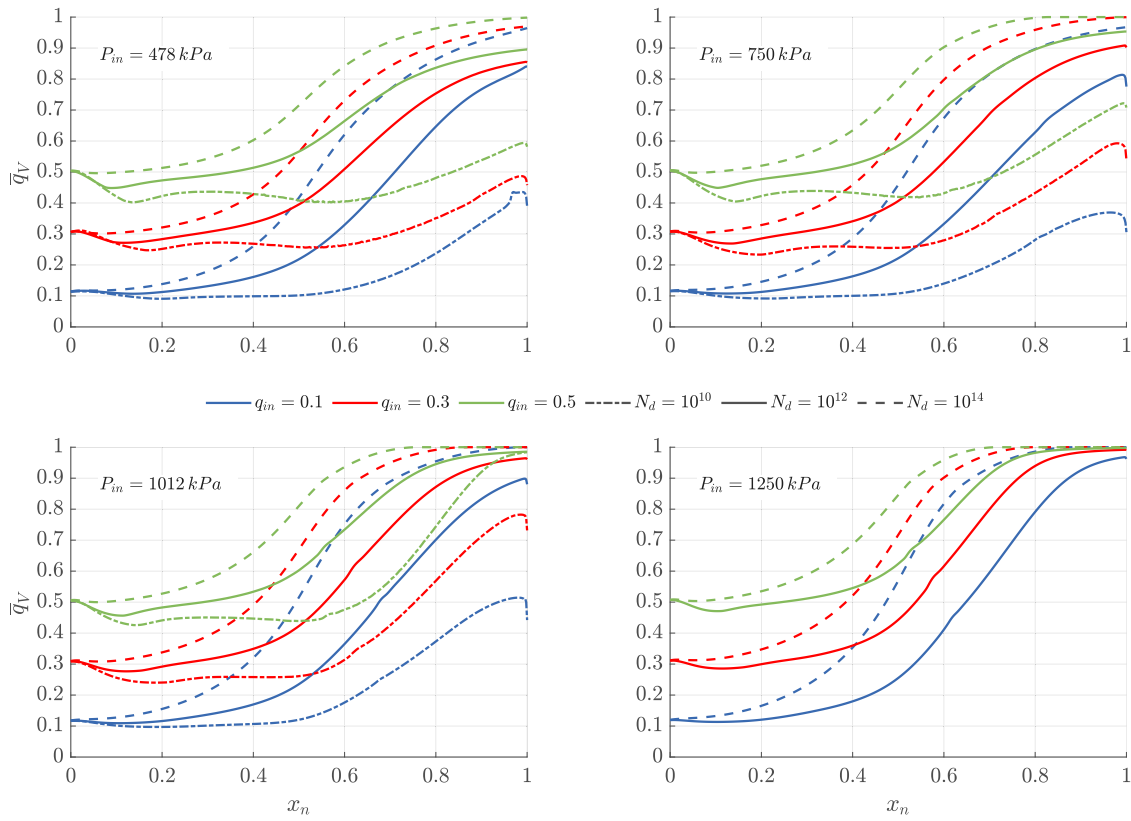
Fig. 9. Streamwise variation of average vapour mass fraction $\bar{q}_V$ for twelve wet-to-dry expansions from four different inlet pressures P_{in}: 478, 750, 1012 and 1250 kPa, and from three different vapour inlet qualities: 0.1, 0.3 and 0.5. The variation of $\bar{q}_V$ for each expansion case has been shown for three different droplet density numbers N_d: 10^{10}, 10^{12} and 10^{14}.
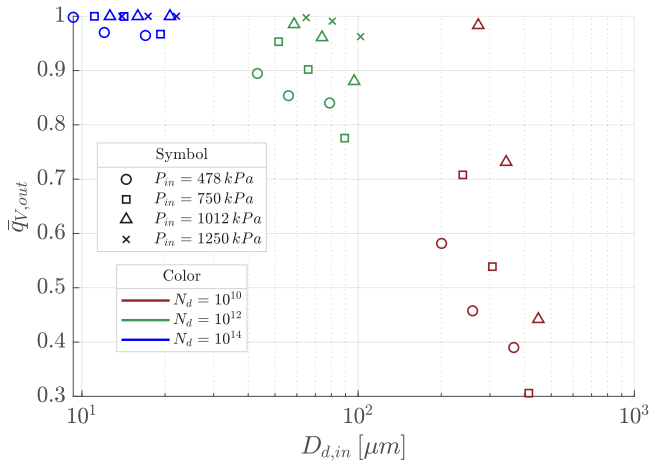
Fig. 10. The relationship between average outlet vapour quality $\bar{q}_V$ and inlet droplet diameter $D_{d,in}$ for all the simulated expansion cases and droplet density numbers; for a given P_{in}–N_d pair, smaller droplets correspond to higher inlet quality.

mass fraction at the outlet (except for the expansion from 1012 kPa and $q_{V,in} = 0.5$). For $N_d = 10^{12}$, the initial droplet size range reduces to around 40–100 μm and the mixture can evaporate more effectively, reaching visibly higher outlet quality between 0.8 and 1. For $N_d = 10^{14}$, the inlet diameter drops below 20 μm. For such small droplets, the mixture easily transitions to dry vapour for almost all the investigated conditions (only for low-pressure expansions is there a small amount of liquid present at the outlet).

Finally, referring to Fig. 9, a sudden drop in vapour quality can be seen at the outlet in some cases. This is because in those cases the

fluid is under-expanded, which leads to the development of a shock and sudden acceleration at the nozzle outlet to meet the imposed boundary condition. Although the volume fraction of vapour slightly increased through the shock, a significant drop in vapour density caused a vapour quality decrease. Ultimately, this shockwave is the result of designing the nozzle under the assumption of homogeneous-thermal equilibrium.

5.1.1. Significance of droplet size

Generally, the results presented in Figs. 9 and 10 indicate that the droplet size is the most dominant factor when it comes to the mixture evaporation rate. The reason behind this becomes clear when analysing the heat-transfer rate between the droplet and the interface:

$$\dot{Q}_L = \mathfrak{H}_L A_{int} \left(T_{int} - T_L \right) \tag{4}$$

Using the definitions of the interfacial area (Eq. (1)) and the Nusselt number, the heat transfer between the droplet and the interface can be expressed as:

$$\dot{Q}_L = \frac{6 N u_L \lambda_L \alpha_L \left(T_{int} - T_L \right)}{D_d^2} \tag{5}$$

Since $N u_L$ in this study is assumed constant, while the change in λ_L is relatively small compared to the change in droplet diameter and liquid superheat level, the heat transfer on the liquid side $\dot{Q}_L$ for a given liquid volume fraction α_L will be proportional to the ratio of the liquid superheat to the square of the droplet diameter:

$$\frac{\dot{Q}_L}{\alpha_L} \propto \frac{T_{sup,L}}{D_d^2} \tag{6}$$

where $T_{sup,L}$ is $T_{int} - T_L$. To visualise how the numerator and denominator of this expression vary with droplet number, these have been plotted in Fig. 11. The plots show the ratios of these parameters obtained with $N_d = 10^{10}$ to the values obtained with $N_d = 10^{12}$ for the expansion
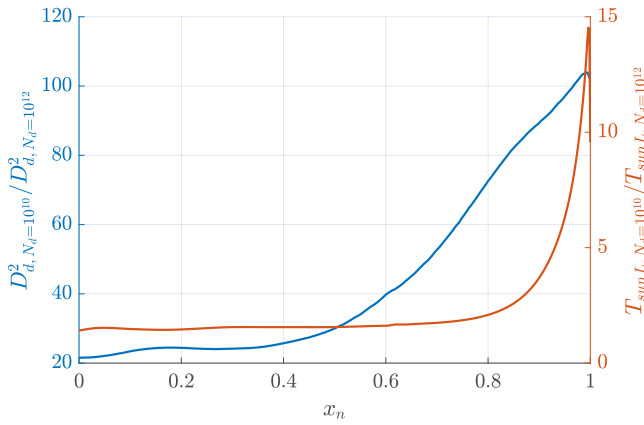
Fig. 11. Streamwise variation of the ratios of droplet diameter square and liquid superheat; the lines represent the ratios of the values obtained with $N_d = 10^{10}$ to the values obtained with $N_d = 10^{12}$ for the expansion from 1012 kPa and inlet quality of 0.3.

from $P_{in} = 1012$ kPa and $q_{in} = 0.3$. Looking at Fig. 11, one can start to understand why the evaporation rate is higher when the droplet number is larger. The square of droplet diameter is at least an order of magnitude higher at $N_d = 10^{10}$, compared to $N_d = 10^{12}$. On the other hand, the liquid superheat level is only about twice of that predicted when $N_d = 10^{12}$ throughout most of the expansion. The heat transfer rate is therefore substantially reduced in case of $N_d = 10^{10}$ (Eq. (6)). One can notice a sudden increase in liquid superheat near the nozzle outlet; this occurs because for $N_d = 10^{12}$ liquid droplets evaporate quicker, diminish in size, and approach the saturation conditions. As the droplets cannot effectively exchange heat in the case of $N_d = 10^{10}$, they remain highly superheated throughout the expansion, causing the ratio of liquid superheat to rapidly increase near the outlet.

5.2. Design and simulated expansion

To help assess the fluid's capability to expand to the design outlet conditions two parameters have been introduced, namely β_p and β_u. The first is the ratio of the pressure drop across the nozzle to the design pressure drop:

$$\beta_p = \frac{P_{in} - P_{out}}{P_{in} - P_{design,out}} \qquad (7)$$

where $P_{design,out}$ is the design outlet pressure. The second parameter is defined as the ratio of mixture velocity to the design outlet velocity:

$$\beta_u = \frac{u_{mix,out}}{u_{design,out}} \qquad (8)$$

where $u_{design,out}$ is the design outlet velocity. Mass-averaged values of pressure and mixture velocity were used when calculating the β parameters. Referring back to Fig. 9, a shock at the outlet was observed in some cases. For this reason, the values for the outlet velocity and pressure were taken just before the actual nozzle outlet to consider the flow conditions prior to the shock when assessing the flow's ability to reach the design values (see Fig. 12).

As expected, the mixture velocity is significantly lower in expansions characterised by larger inlet droplets. The cause of this is two-fold; on the one hand delayed evaporation implies higher mixture density and lower mixture velocity. On the other hand, larger droplets contribute to increased drag force, interphase friction and energy loss, which lead to a reduction in the mixture velocity. For the same reason, the outlet pressure deviated from the design values. These effects gradually diminish as the droplet number increases. The discrepancy between the design and simulated outlet conditions emphasises the need for an appropriate nozzle design tool that can account for non-equilibrium

effects, rather than using a homogeneous-equilibrium model to generate the nozzle, as was the case in this work. Nonetheless, it is worth repeating that since the main goal of this study was to give further insight into the wet-to-dry expansion characteristics in a converging–diverging nozzle, rather than develop an optimal nozzle design technique, the nozzle design tool based on the homogeneous-equilibrium flow was deemed suitable for preliminary analysis. In future studies, the performance of more sophisticated design methods such as the quasi-1D non-equilibrium design tool developed by White [32], will be evaluated.

5.3. Significance of non-equilibrium effects

Sections 5.1 and 5.2 indicate that the two-fluid model predictions may seriously deviate from the homogeneous-equilibrium model predictions for lower droplet numbers. Fig. 13 explicitly shows the extent of mechanical and thermal non-equilibrium for the expansions from 478 kPa and 1012 kPa. The level of mechanical inhomogeneity is represented by a relative velocity slip $u_{slip,rel}$ which is the velocity slip normalised by mixture velocity: $u_{slip,rel} = (u_V - u_L)/u_{mix}$. The thermal non-equilibrium is expressed as the temperature difference between the phases normalised by the saturation temperature: $\Delta T_{LV,rel} = (T_L - T_V)/T_{sat}$. When computing $\Delta T_{LV,rel}$, temperatures were kept in Celsius degrees. Looking at the average velocity slip (Fig. 13) it is observed that for $N_d = 10^{14}$, $\bar{u}_{slip,rel}$ is relatively small, with a peak value below 10%. Reducing droplet number increases the slip; for $N_d = 10^{12}$ the slip is between 15%–25% throughout most of the nozzle length. The velocity slip further increases to about 30%–60% for $N_d = 10^{10}$. In absolute values, the velocity difference is below 10 m/s for the highest droplet number, around 10–20 m/s for the intermediate droplet number and about 20–50 m/s for the lowest droplet number. It could therefore be concluded that the mechanical non-equilibrium becomes significant when the droplet number is below 10^{14}. It is worth noting that the relative slip is generally higher in the case of lower-pressure expansions. Looking at Fig. 10 it can be seen that for the same droplet number, the expansion from higher pressure is associated with larger inlet droplet size. Therefore, one might expect that at the beginning of the expansion, the relative slip should be higher for the higher-pressure case. The inverse is observed, which is the effect of a smaller density difference between the vapour and liquid at elevated pressures. For example, the ratio of saturated-liquid density to saturated-vapour density at 478 kPa is about 22; this reduces to around 8 when the pressure is raised to 1012 kPa. The reduced density difference contributes to better mechanical homogeneity of the two-phase flow.

To understand the development of thermal non-equilibrium it should be first understood that negative values of $\Delta T_{LV,rel}$ signify areas where liquid's temperature is lower than that of vapour, while the interface temperature T_{int} is identical to the local saturation temperature. Generally, it was expected that flows characterised by large droplets would have highly superheated liquid phase due to its reduced capability to give out heat to the interface and vaporise (see. Eq. (6)). This effect should gradually diminish as the droplet number is raised, expecting the liquid's temperature to approach vapour temperature, reducing thermal non-equilibrium. This, to some extent, can be observed in Fig. 13, where the liquid superheat for $N_d = 10^{10}$ remains relatively high throughout the expansion. On the other hand, the thermal non-equilibrium gets smaller when N_d is raised; however, one can see that in these cases, liquid can develop a considerable negative $\Delta T_{LV,rel}$ in the diverging section of the nozzle, near the end of the expansion. Large negative values of $\Delta T_{LV,rel}$ typically correspond to axial positions characterised by high vapour qualities, i.e. extremely low liquid volume fractions and extremely small droplets. These areas could represent superheated gas flows containing tiny droplets that did not manage to fully vapourise. Despite T_L being lower than T_V, evaporation continues as indicated by Fig. 9. To better understand this phenomenon, one could refer back to Eq. (2), and assume that vapour
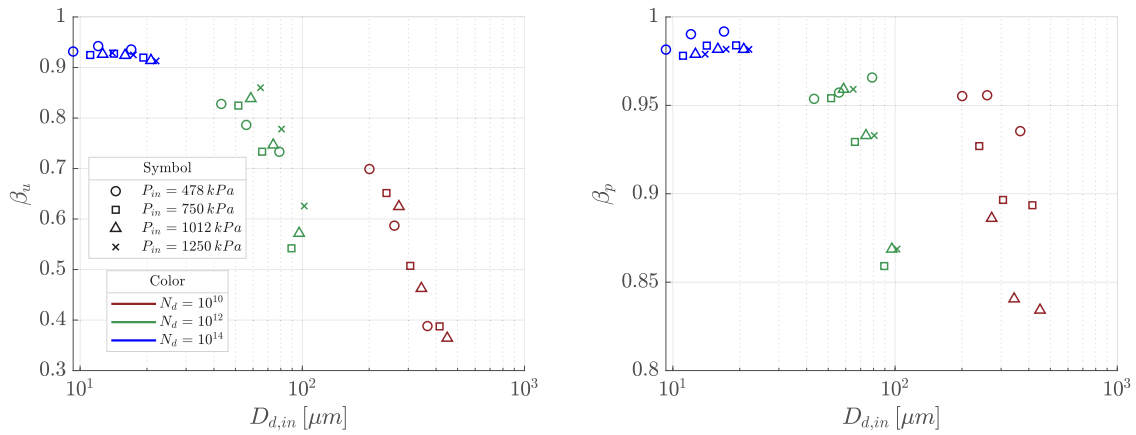
Fig. 12. The relationship between the inlet droplet diameter $D_{d,in}$ and the β parameters; β_p is the ratio of the pressure drop to the design pressure drop, while β_u is the ratio of the mixture outlet velocity to the design outlet velocity.
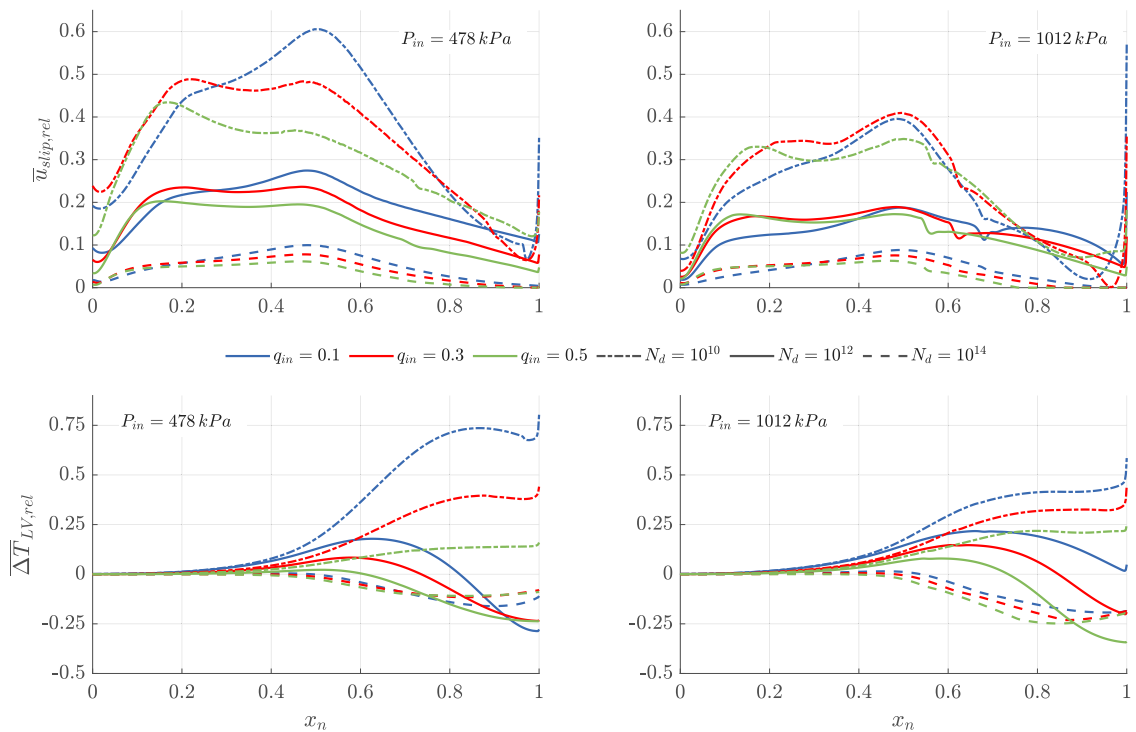
Fig. 13. Streamwise variation of average relative velocity slip $\overline{u}_{slip,rel}$ and average relative thermal non-equilibrium $\overline{\Delta T}_{LV,rel}$ in the expansions from 478 kPa and 1012 kPa, with three inlet qualities $q_{V,in}$ of 0.1, 0.3 and 0.5 and three different droplet density number N_d of 10^{10}, 10^{12} and 10^{14}; $\overline{u}_{slip,rel}$ is the velocity slip normalised by the mixture velocity, while $\overline{\Delta T}_{LV,rel}$ is temperature difference between the phases normalised by the saturation temperature.

remains saturated throughout the expansion, i.e. $T_V = T_{int}$. Such an assumption was made in previous numerical studies of flash boiling of water [44,51]. As the fluid expands, the liquid is expected to get superheated before boiling initiates. This would then imply that the numerator of Eq. (2) becomes negative when boiling takes place. In this study, T_V could not be fixed to the saturation conditions as this would prevent vapour from becoming superheated. Nevertheless, one should expect that the same rule applies to the wet-to-dry expansion, i.e. boiling is expected when the numerator of Eq. (2) is negative. Therefore, even if $T_L < T_V$, but both phases remain superheated or vapour develops sufficient superheat, the mixture would continue to evaporate, and the numerator of Eq. (2) would remain negative. In summary, the regions where T_L remains above T_V can be thought of as the regions where superheated liquid droplets travel in cooler vapour, and vaporise giving off heat to the surrounding vapour. On the other hand, the regions where T_L drops below T_V can be thought of

as the regions where tiny droplets travel in superheated vapour, and vaporise by being heated up by the surrounding hot vapour. Although, this could explain the physical process of boiling in both conditions, the authors found that in some cases, both liquid and vapour phases became superheated in relatively early stages of expansion. Since these areas would correspond to the two-phase regime under equilibrium conditions, it is expected that if the phases are given sufficient time they should reach the saturation conditions. However, if both phases have temperatures above the saturation level, it is unclear how they could ever reach the saturation temperature by exchanging heat. This is not fully understood by the authors and requires further investigation.

As for the quantitative evaluation of the thermal non-equilibrium, the absolute temperature difference between the phases reached about 50–60 °C in case of $N_d = 10^{10}$ and up to around 30 °C in case of higher N_d. However, it should be remembered that the temperature difference is probably more important in case of large droplets as it

signifies the inability of liquid to give off heat and effectively evaporate. In case of small droplets, large temperature differences would typically correspond to the areas where extremely small liquid droplets travel in the superheated vapour — the areas of extremely small volume fractions of liquid. Since the volume fraction is extremely small, one could imagine that these areas could also be more prone to numerical errors, which also requires further investigation.

Overall, it can be said that when simulating wet-to-dry expansion of MM, there can be a large difference in velocities and temperature of vapour and liquid phases, and neglecting non-equilibrium effects could lead to significant inaccuracies.

5.4. Flow uniformity

Apart from assessing average flow properties, it is also important to investigate whether at a given streamwise location flow properties are uniform across the nozzle. Flow uniformity may be particularly important when the wet-to-dry nozzle forms part of a turbine stator. For example, the overall vapour quality could be high, while a small amount of liquid concentrated in one area in the form of a streak or film could impinge on the rotor blades. This could possibly entail erosion issues, increased wear rates and lead to performance deterioration.

5.4.1. Phase separation

Fig. 14(a) and (b) depict the two-dimensional variation of vapour mass fraction across the nozzle for the expansions from 478 kPa and 1012 kPa, both with an inlet quality of 0.3. Although the two nozzles have different lengths, with the one designed for the 1012 kPa expansion being shorter, the longer nozzle has been scaled to facilitate easier visual assessment of the flow field. As the fluid is accelerated through the converging section of the nozzle, the flow is turned towards the nozzle core (or the centre line of the nozzle). Liquid droplets, having a higher density than the surrounding vapour, require more time to adjust to the changing flow direction (i.e., they are characterised by longer relaxation times), and instead of immediately adjusting to the main flow direction, droplets tend to continue along their flow path. This results in the accumulation of the liquid phase near the wall in the converging part of the nozzle. The situation is reversed past the throat; the flow is now being turned away from the nozzle core. For the same reasons described above, liquid droplets tend to continue on their path, creating a characteristic core flow region, as visible in Fig. 14, while the area in the proximity of nozzle walls is occupied by the vapour alone. The phase separation is more pronounced at lower N_d due to the higher inertia of larger liquid droplets, which translates to longer relaxation times and reduced capability to follow the mean flow. As for the effect of inlet pressure, the separation appears to be more pronounced for the lower-pressure case. The reason for this is two-fold; as discussed before, the density difference between the liquid and vapour phases is higher at lower pressures, which enhances mechanical inhomogeneity. Moreover, the evaporation rate is higher in case of the 1012 kPa expansion, which means that the droplets evaporate quicker and are likely to be smaller at a given streamwise location comparing to the 478 kPa expansion; smaller droplets have lower inertia, shorter relaxation times and higher capability to follow the mean flow. Summarising Fig. 14(a) and (b) it can be concluded that the lower the droplet number (or in other words the larger the droplets) and the lower the inlet pressure, the higher the flow non-uniformity in terms of the transverse separation of the phases.

5.4.2. Velocity variation

Fig. 14(c) and (d) show two-dimensional variations of mixture velocity corresponding to the expansions depicted in Fig. 14(a) and (b) respectively. The velocity is relatively uniform in the converging section; velocity in that area is very low and spatial uniformity is of little concern. The transverse variations in velocity become important in the diverging section; u_{mix} in the proximity of the wall is visibly

higher than in the core of the nozzle. Generally, the velocity of the liquid phase is lower than that of the vapour due to higher density. For a given pressure gradient applied to the control volume, the droplets will develop lower velocity. Hence, the overall velocity in a given control volume is lower when it contains more liquid in relation to the control volume with lower liquid content. Lower liquid velocity also contributes to the development of drag force between the phases, such that the vapour phase is slowed down by the suspended droplets. This is why, in the region close to the wall where there is almost pure vapour, the velocity tends to be higher than in the core of the nozzle where there is a significant amount of liquid present. As the transverse separation of phases is higher for lower N_d and lower pressure, so is the velocity non-uniformity in these conditions.

To provide a more quantitative measure of flow uniformity at the nozzle outlet, normalised standard deviations of outlet vapour mass fraction and mixture velocity have been calculated for all the simulated expansions. In order to calculate the standard deviations, the nozzle outlet was discretised into 500 points and q_V and u_{mix} data have been retrieved at each point. Using this data standard deviations were calculated and normalised by the mean values of outlet quality and mixture velocity. Fig. 15 presents the variation of the normalised standard deviations with the droplet inlet diameter for all the expansion cases. For all inlet conditions, the flow leaving the nozzle appears to be highly non-uniform when the inlet droplet diameter is between 200–450 μm ($Nd = 10^{10}$), with σ_q and σ_u being in the range of 20%–50% and 15%–32% of the mean values respectively. This is not surprising having observed how the flow behaviour changes as the droplet number decreases (see Fig. 14). Once $D_{d,in}$ falls to about 40–100 μm ($Nd = 10^{12}$), the normalised standard deviation for both the outlet quality and mixture velocity drops below 10% in most cases. For inlet droplet diameter below 20 μm ($Nd = 10^{14}$), the standard deviation of q_V is practically negligible, while for the mixture velocity, it does not exceed several percent. A visual assessment of the two-dimensional variation of u_{mix} and q_V presented in Fig. 14 suggests that the two-expansions with lower droplet numbers and lower inlet pressure tend to be less uniform; this is well reflected assessing the standard deviations for all the studied cases, which also indicates that for a given inlet droplet diameter the flow is more uniform for higher-pressure expansions. This was also noted and explained when discussing Fig. 14.

In summary, wet-to-dry expansions appear to be highly non-uniform when the mixture is characterised by droplet numbers below 10^{12} and larger droplet sizes. The flow's uniformity quickly increases with the droplet number such that it may be deemed negligible for an inlet droplet diameter below 20 μm.

5.5. Comment on the initial conditions

It is clear that the mixture evaporation is strongly affected by the droplet size. Other factors affecting the vapourisation rate are the inlet pressure and inlet quality. The inlet conditions have little impact on the vapour quality at the nozzle outlet as long as N_d is sufficiently high; i.e. when the droplet inlet diameter was below 20 μm. Nonetheless, when N_d is reduced and droplets get larger, the inlet conditions begin to play an important role, which becomes evident looking at Fig. 10. In general, the results show that the fluid can reach dry conditions more easily when expanding from higher pressures and higher inlet qualities. This could be anticipated when looking at Fig. 4, which indicates that under isentropic homogeneous-equilibrium conditions, the vapour develops higher superheat at the outlet for the expansions from higher pressures and qualities. On the other hand, the fluid expanding from lower pressures are barely able to escape the two-phase dome. Hence, one can imagine that for high-pressure expansions, even if the evaporation is delayed with respect to the ideal conditions shown in Fig. 4, the fluid could still cross the saturated-vapour curve, whereas for lower-pressure expansions this would probably lead to wet outlet conditions. Therefore, from the point of view of the nozzle
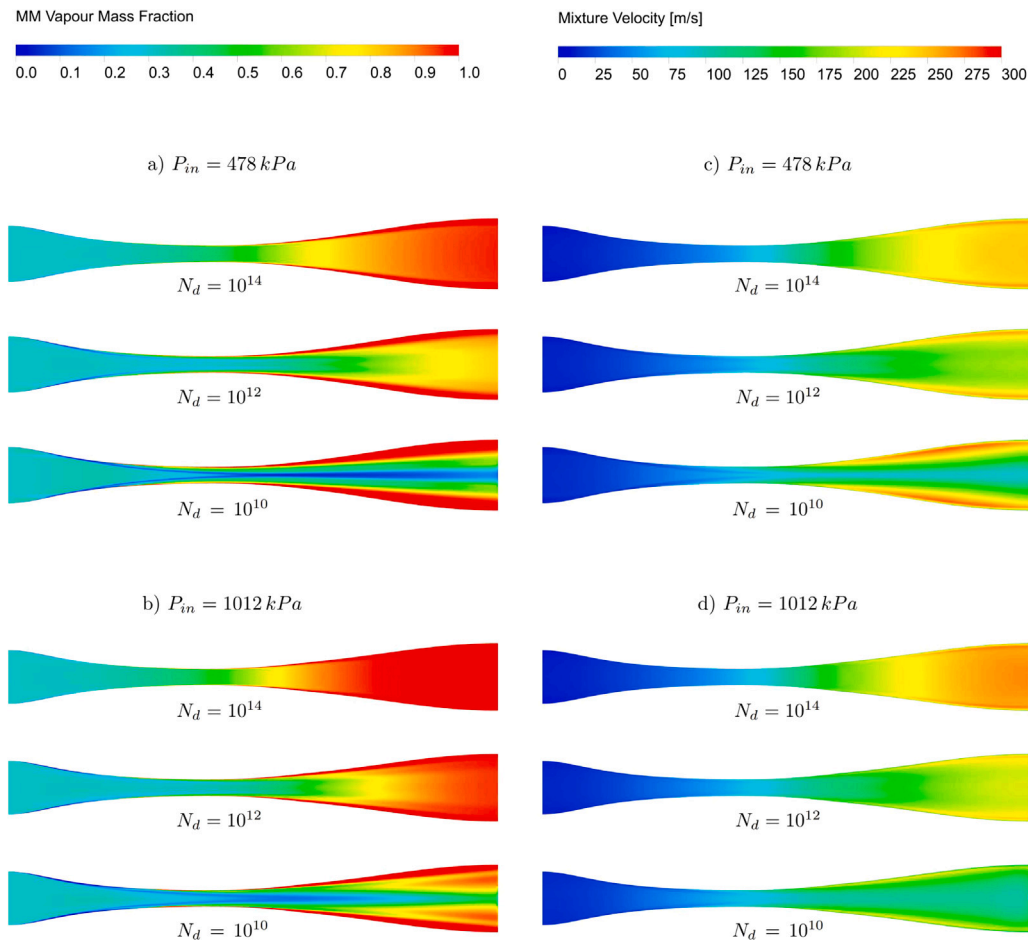
Fig. 14. Two-dimensional variations of vapour mass fraction and mixture velocity within the nozzle.
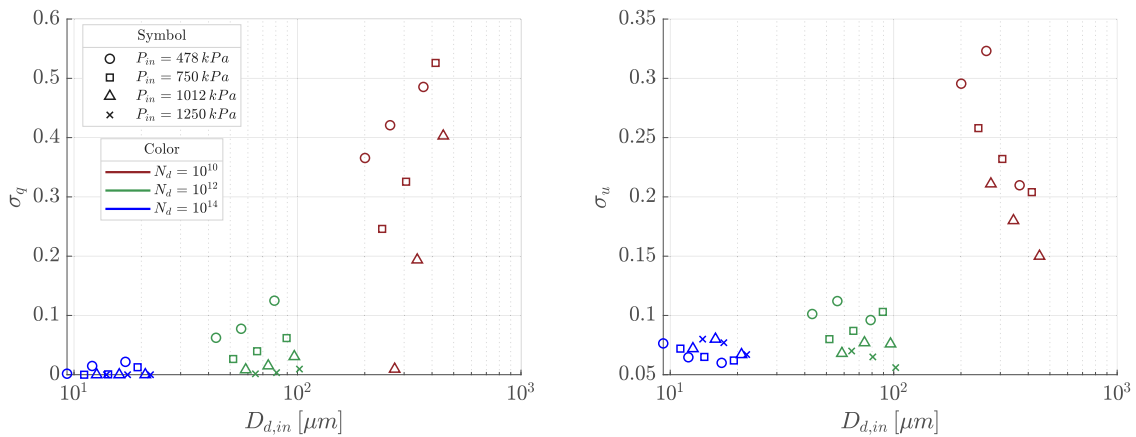
Fig. 15. The relationship between the inlet droplet diameter and normalised standard deviations of vapour mass fraction (σ_q) and mixture velocity (σ_u) across the nozzle outlet; the standard deviations were normalised by mean outlet values of q_V and u_{mix}.

design, it seems advisable to expand the fluid from the highest possible pressure and inlet quality. Nevertheless, from a thermodynamic point of view, the higher the inlet pressure and vapour quality, the smaller the relative advantage of two-phase expansion compared to single-phase ORC systems. White [8] found that for an open heat source with inlet temperature of 150 °C a two-phase ORC could generate around 30% more power than a single-phase cycle. The power improvement reduced to around 15% and 3% when the heat source temperature was raised to 200 and 250 °C respectively. Looking at the wet-to-dry cycle

diagram in Fig. 1, it is obvious that the heat source inlet temperature must be higher than the saturation temperature of the mixture entering the expander. The saturation temperatures corresponding to 478, 750, 1012 and 1250 kPa are 164.8, 188.4, 205.5 and 218.2 °C respectively. It then becomes clear why lower pressures are more attractive from the thermodynamic point of view. White's study [8] also showed that the relative increase in power output diminishes as the inlet vapour quality increases, which is simply due to the fact that as the inlet quality increases, the cycle gradually approaches the single-phase architecture
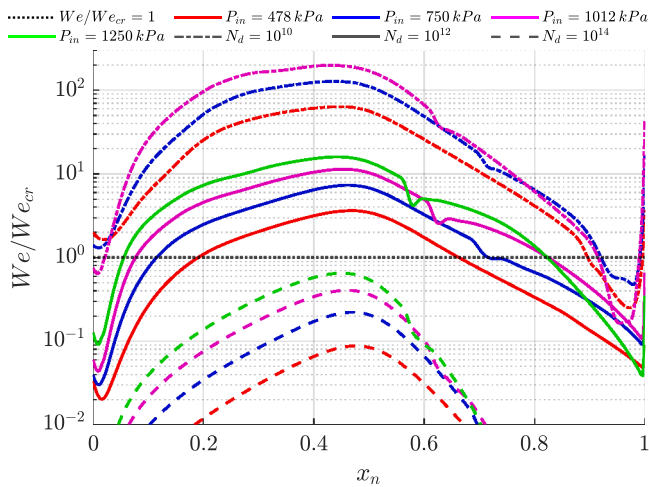
Fig. 16. The streamwise variation of the ratio of the average Weber number to the critical Weber number; droplet breakup is expected to occur if the ratio We/We_{cr} exceeds unity. The mixture was expanded from inlet quality of 0.3 for each presented case.

and the change between these two gradually diminishes. However, it should also be highlighted that expanding the fluid from very low qualities may lead to extremely large volumetric expansion ratios that could affect the turbine design and performance. Therefore, when designing the wet-to-dry cycle integrated with a radial-inflow turbine, there will likely be a trade-off between the thermodynamic performance and the feasibility of the turbine design.

6. Droplet breakup

As has been presented, the capability of the two-phase mixture to evaporate and turn into uniform vapour flow is primarily dependent on the droplet size. In the absence of experimental data, it is difficult to estimate a definite number for the droplet diameter, and instead, a range of values can be studied. The upper limit of N_d is not critical as the solution tends to approach the homogeneous-equilibrium model and the mixture can easily evaporate. However, the minimum droplet size is critical to the evaporation rate and flow uniformity. Hence, it seems necessary to estimate the minimum droplet size. This can be done by assessing the Weber We and Ohnesorge Oh numbers, which can be defined as:

$$We = \frac{\rho_V \left(u_V - u_L\right)^2 D_d}{\sigma} \tag{9}$$

$$Oh = \frac{\mu_L}{\sqrt{\rho_L D_d \sigma}} \tag{10}$$

where σ and μ_L are the surface tension coefficient and the liquid dynamic viscosity. The Weber number represents the ratio of the aerodynamic drag force that acts to distort and fragment the droplet to the surface tension force that resists the fragmentation. The Ohnesorge number denotes the ratio of viscous to surface tension forces. The two non-dimensional parameters have been widely used in secondary atomisation studies. Various experimental studies summarised by Guildenbecher et al. [67] agree that for $Oh < 0.1$ the critical Weber number We_{cr} (i.e. the Weber number at which droplet breakup is expected to begin) is independent of the Oh number. For higher Oh, different correlations have been proposed to define We_{cr}, such as the one proposed by Bordkey [68]:

$$We_{cr} = We_{cr, Oh \to 0} \left(1 + 1.077 Oh^{1.6}\right) \tag{11}$$

where $We_{cr, Oh \to 0}$ is the critical Weber number as Oh tends to zero, which as mentioned can be generally considered to be about 11. Fig. 16

illustrates the streamwise variation of the average ratio of the Weber number to the critical Weber number We/We_{cr}. The ratio We/We_{cr} has been shown for all investigated pressures. The inlet quality was fixed to 0.3 for each case, although similar trends were observed for other inlet qualities. The location at which We exceeds We_{cr} marks the location of the anticipated onset of droplet breakup. It is observed that for $N_d = 10^{14}$ the Weber number ratio is below unity for all the pressure levels, which means that droplet breakup is not anticipated. However, for $N_d = 10^{12}$, We/We_{cr} is typically between 1–10 through much of the expansion. The ratio further increases by around one order of magnitude as the droplet number is reduced to 10^{10}. In summary, droplet breakup is expected to take place when $N_d \leqslant 10^{12}$. This means that even though the mixture could not effectively evaporate at lower droplet numbers, and the flow exhibits highly non-uniform outlet conditions, it could be anticipated that the expansion characteristics would change if the droplet breakup effects are taken into account. It was shown that the delayed evaporation is primarily caused by the inability of larger droplets to give out heat to the interface; therefore, if the larger droplets were to fragment into a number of smaller droplets, the evaporation rate can be potentially enhanced. The effect of droplet breakup is to be further investigated in future studies.

7. Conclusions

In this study, a two-fluid model has been used to simulate the wet-to-dry expansion of siloxane MM in a planar converging–diverging nozzle, where both thermal and mechanical non-equilibrium effects are considered. The model was validated against experimental data for the flash boiling of water. Various boundary conditions have been investigated with inlet pressure ranging from 478 kPa to 1250 kPa and inlet vapour quality from 0.1 to 0.5. The size of the droplets was modelled using a constant number of droplets per unit volume, which varied between 10^{10} and 10^{14}. The main conclusions of this study can be summarised as follows:

- A sensitivity study showed an acceptably small deviation in the solution when alternative interphase models were used, which gives extra confidence in the reliability of the setup.
- The decisive factor influencing the phase change process was the droplet diameter; for small inlet droplet diameter below 20 μm ($N_d = 10^{14}$), the mixture completely evaporated in almost all investigated cases. For inlet droplet diameters between 40–100 μm ($N_d = 10^{12}$), the outlet vapour mass fraction was between 80%–100% and this reduced to between 40%–75% for droplet diameters between 200–450 μm ($N_d = 10^{10}$).
- The significance of mechanical and thermal non-equilibrium effects predominantly depends on droplet size. The homogeneous-equilibrium model is valid only for inlet droplet diameter below 20 μm; for larger droplets the velocity slip and phase temperature difference become too large to be neglected.
- Generally, expansions from higher inlet pressures and vapour qualities can more readily reach the design outlet conditions and fully evaporate. However, such cases are also associated with a reduced relative advantage of two-phase cycles compared to single-phase architectures.
- Significant flow non-uniformity, measured in terms of the standard deviation of vapour quality and mixture velocity, was observed for large droplets. For $N_d = 10^{10}$ the standard deviation of the outlet quality ranged between 20 and 50% of the mean, while the standard deviation of the mixture velocity ranged between 15%–30% of the mean. The flow non-uniformity quickly diminished as the droplet number was raised, with fairly uniform flow at $N_d = 10^{14}$. Higher pressures were characterised by better flow uniformity, which is due to smaller interphase density differences and quicker evaporation.

- Droplet breakup analysis indicates that breakup is likely to occur for droplet numbers smaller than 10^{14}, which could enhance the evaporation rate.

Further research is necessary to integrate a droplet breakup model within the simulation to predict the realistic size of the droplets. More sophisticated nozzle design tools, accounting for non-equilibrium effects, should also be evaluated in future studies. Finally, experimental work is required to validate these findings.

Declaration of competing interest

The authors declare that they have no known competing financial interests or personal relationships that could have appeared to influence the work reported in this paper.

Data availability

Data will be made available on request.

Acknowledgements

Appendix A. Two-fluid model

A.1. Governing equations

The conservation equations for the flashing two-phase flows are formulated similarly to single-phase flows, with two main differences. Firstly, each control volume can be occupied by both phases simultaneously; each term in the governing equation is therefore multiplied by the volume fraction of the corresponding phase. Secondly, the phases can exchange mass, momentum and energy, which requires the addition of source/sink terms in each transport equation.

The mass continuity equations for the liquid and vapour phases are:

$$\frac{\partial (\alpha\,\rho)_L}{\partial t} + \nabla \cdot \left(\alpha\rho\vec{U} \right)_L = \left(\dot{m}_{VL} - \dot{m}_{LV} \right) \tag{12a}$$

$$\frac{\partial (\alpha\,\rho)_V}{\partial t} + \nabla \cdot \left(\alpha\rho\vec{U} \right)_V = \left(\dot{m}_{LV} - \dot{m}_{VL} \right) \tag{12b}$$

where ρ and $\vec{U}$ represent phase density and velocity, while α is the phase volume fraction. The subscripts L and V correspond to liquid and vapour phases respectively, whilst $\dot{m}_{VL}$ and $\dot{m}_{LV}$ represent the mass transfer from vapour to liquid and from liquid to vapour respectively.

The momentum conservation equations are given as:

$$\begin{aligned} \frac{\partial \left(\alpha\rho\vec{U} \right)_L}{\partial t} + \nabla \cdot \left(\alpha\rho\vec{U}\vec{U} \right)_L \\ = -\alpha_L\,\nabla P + \nabla \cdot \tau_L + \left(\dot{m}_{VL}\vec{U}_V - \dot{m}_{LV}\vec{U}_L \right) + M_L \end{aligned} \tag{13a}$$

$$\begin{aligned} \frac{\partial \left(\alpha\rho\vec{U} \right)_V}{\partial t} + \nabla \cdot \left(\alpha\rho\vec{U}\vec{U} \right)_V \\ = -\alpha_V\,\nabla P + \nabla \cdot \tau_V + \left(\dot{m}_{LV}\vec{U}_L - \dot{m}_{VL}\vec{U}_V \right) + M_V \end{aligned} \tag{13b}$$

where the stress tensor τ for the given phase is expressed as:

$$\tau = \mu \left(\nabla\vec{U} + \left(\nabla\vec{U} \right)^T - \frac{2}{3}\delta\,\nabla \cdot \vec{U} \right) \tag{14}$$

Since the two phases have different velocity fields, there is a momentum exchange M_L and M_V through interfacial forces. Since the force exerted by the liquid phase onto the vapour phase is equal and opposite

to the force exerted by the vapour phase onto the liquid phase it follows that $M_L = -M_V$. In addition to that, momentum will be carried from one phase to the other due to mass transfer, which is accounted for by the terms $\dot{m}_{VL}\vec{U}_V$ and $\dot{m}_{LV}\vec{U}_L$. The pressure vector P has no phase subscript because it is assumed that the phases have identical pressures.

Eqs. (15a) and (15b) are the energy conservation equations formulated in terms of total enthalpy. Energy is exchanged between the phases by mass and heat transfer. Energy transfer associated with the mass transfer is accounted for by the terms $\dot{m}_{LV}h_{tot,L}$ and $\dot{m}_{VL}h_{tot,V}$, while $\dot{q}_V$ and $\dot{q}_L$ represent the heat transfer rate on the vapour and liquid side of the interface respectively. T and λ are phase temperature and thermal conductivity.

$$\begin{aligned} \frac{\partial \left(\alpha\rho h_{tot} \right)_L}{\partial t} + \nabla \cdot \left(\alpha\rho\vec{U}h_{tot} \right)_L = \alpha_L\frac{\partial P}{\partial t} + \nabla \cdot (\alpha\lambda\,\nabla T)_L \\ + \nabla \cdot \left(\vec{U}\tau \right)_L + \left(\dot{m}_{VL}h_{tot,V} - \dot{m}_{LV}h_{tot,L} \right) + \dot{q}_L \end{aligned} \tag{15a}$$

$$\begin{aligned} \frac{\partial \left(\alpha\rho h_{tot} \right)_V}{\partial t} + \nabla \cdot \left(\alpha\rho\vec{U}h_{tot} \right)_V = \alpha_V\frac{\partial P}{\partial t} + \nabla \cdot (\alpha\lambda\,\nabla T)_V \\ + \nabla \cdot \left(\vec{U}\tau \right)_V + \left(\dot{m}_{LV}h_{tot,L} - \dot{m}_{VL}h_{tot,V} \right) + \dot{q}_V \end{aligned} \tag{15b}$$

Contrary to single-phase flows, an additional conservation equation is solved for the volume fraction, which states that the sum of vapour and liquid volume fractions in each control volume must add up to unity.

$$\alpha_L + \alpha_V = 1 \tag{16}$$

A.2. Interphase models

The two-fluid model has the advantage of being a more general approach to modelling flashing flows in the sense that it can be applied to a wide range of problems without the need for empirical tuning. The reliability of the model however depends on the selection and accuracy of interphase models. It is up to the researcher to know which models are best suited to the given application. If one does not have confidence in the employed interphase models, the two-fluid model may generate misleading results and be less accurate than simplified models such as the homogeneous-equilibrium model. The details of the interphase models employed in simulating the wet-to-dry expansion are given below.

The mass transfer is assumed to result from the interphase heat transfer, which is evaluated using the two-resistance model. The model assumes an interface between the continuous and dispersed phases, which is at local thermodynamic equilibrium conditions (i.e., saturation conditions). The heat transfer occurs between the phases and the interface separately, such that there are two distinct heat-transfer coefficients for each phase that determine the heat transfer rate between the phases and the interface. The interfacial heat fluxes are defined as:

$$\dot{q}_L = \mathfrak{H}_L \left(T_{int} - T_L \right) \tag{17a}$$

$$\dot{q}_V = \mathfrak{H}_V \left(T_{int} - T_V \right) \tag{17b}$$

where $\mathfrak{H}_L$ and $\mathfrak{H}_V$ are heat transfer coefficients for the liquid and vapour sides respectively, while T_{int} is the interfacial temperature, equal to the local saturation temperature. Knowing that the interface is capable of storing neither mass nor energy, the energy balance applied to the interface must be zero:

$$\dot{q}_L A_{int} + \dot{m}_{VL}h_V + \dot{q}_V A_{int} + \dot{m}_{LV}h_L = 0 \tag{18}$$

The first two terms in Eq. (18) $\left(\dot{q}_L A_{int} + \dot{m}_{VL}h_V \right)$ represent the energy supplied to the liquid phase; $\dot{q}_L A_{int}$ is the energy associated with the heat transfer and $\dot{m}_{VL}h_{LV}$ is the energy associated with the mass transfer (from the interface to the liquid phase). Similarly, the last two terms in Eq. (18) represent the energy exchange between the interface and the vapour phase. Substituting Eqs. (17a)–(17b) in Eq. (18), and using the fact that the mass transferred from the liquid phase to the

interface is equal to the mass transfer from the interface to the vapour phase ($\dot{m}_{LV} = \dot{m}_{VL}$), one can derive the following equation, defining the evaporation rate [61]:

$$\dot{m}_{LV} = -\dot{m}_{VL} = \frac{\mathfrak{H}_L A_{int} \left(T_{int} - T_L\right) + \mathfrak{H}_V A_{int} \left(T_{int} - T_V\right)}{h_{LV}} \quad (19)$$

In order to implement the phase-change model based on the interfacial heat transfer, heat-transfer coefficients for the liquid and vapour phases need to be evaluated. These heat transfer coefficients are associated with the corresponding Nusselt numbers, Nu_L and Nu_V, based on the droplet diameter D_d and the corresponding thermal conductivity. For estimating the Nusselt number on the continuous side, a range of empirical and analytical correlations exist that account for conduction, convection and turbulence effects. This model uses the Ranz-Marshall [56] correlation, which was derived from experimental tests on a water droplet evaporating in a hot air stream:

$$Nu_V = \frac{\mathfrak{H}_V D_d}{\lambda_V} = 2 + 0.6 Re_d^{0.5} Pr_V^{0.33} \quad (20)$$

where R_d is the droplet Reynolds number based on droplet diameter and slip velocity, while Pr_V is the vapour Prandtl number:

$$Re_d = \frac{D_d \left|\vec{U}_V - \vec{U}_L\right|}{\nu_V} \quad (21)$$

$$Pr_V = \frac{c_{p,V} \mu_V}{\lambda_V} \quad (22)$$

The Nusselt number for the heat transfer between the liquid droplet and the interface is unknown; however, a constant value of 6 can be taken as an approximation derived from the transient heat-transfer analysis in a solid sphere [57].

Although, three major interphase momentum exchange mechanisms were considered in the wet-to-dry expansion study, generally, there are five mechanisms that are distinguished in two-phase flows: drag, lift, turbulent dispersion, wall lubrication and virtual mass forces.

The density difference between the phases causes each phase to have a different acceleration when the same axial pressure gradient is applied. This gives rise to the interfacial drag, which for the particle model is expressed as:

$$F_D = \frac{1}{2} \rho_V A C_D \left(U_V - U_L\right)^2 \quad (23)$$

where A is the projected area upon which the drag force acts, while C_D is the non-dimensional drag coefficient. Since the dispersed phase is in the form of spherical droplets, the total interfacial drag per unit volume can be expressed as:

$$D_{LV} = \frac{3}{4} \frac{C_D}{D_d} \alpha_L \rho_V \left|U_L - U_V\right| \left(U_L - U_V\right) \quad (24)$$

The mixture is expected to rapidly accelerate to high velocities, which may be associated with a significant velocity slip resulting in droplet shape distortion. Therefore, the Ishii-Zuber [58] model was used to evaluate the drag coefficient, which is capable of accounting for shape distortion and the effect of densely distributed particles, making it suitable for flows with both dilute and densely distributed droplets.

The lift force is a force that acts on the dispersed phase in the direction perpendicular to the direction of flow. It is caused by shear effects when there is a rotational movement of the continuous phase (i.e. when the curl of its velocity is non-zero):

$$F_L = \alpha_L \rho_V C_L \left(U_L - U_V\right) \left(\nabla \times U_V\right) \quad (25)$$

The parameter C_L is a non-dimensional lift coefficient, which is evaluated using the Tomiyama [59] model.

Turbulence enhances the distribution of the dispersed phase from regions of high concentration to regions of low concentration of the dispersed phase. Liquid droplets are caught up in turbulent eddies through the interfacial drag force. Favre Averaged Drag was used for estimating the turbulent dispersion, which proved suitable for a wide range of applications [57]:

$$F_{TD} = C_{TD} C_{VL} \frac{\nu_{tV}}{\sigma_{tV}} \left(\frac{\nabla \alpha_L}{\alpha_L} - \frac{\nabla \alpha_V}{\alpha_V}\right) \quad (26)$$

where C_{TD} is a constant defined manually with a value close to unity, C_{VL} is a momentum transfer coefficient for the interphase drag, while σ_{tV} and ν_{tV} are the turbulent Schmidt number and eddy viscosity respectively.

It has been previously noticed that for certain flows, such as bubbly up-flow in a vertical pipe [69], the dispersed phase tends to accumulate near the wall but is not directly adjacent to it. These effects seem particularly relevant for buoyancy-driven flows, where the dispersed phase has a lower or similar density to that of the surrounding medium. In the investigated case, there is a high-speed flow of liquid droplets suspended in vapour with a density at least an order magnitude lower than the droplets. Hence, the wall lubrication effects are deemed negligible, and the droplets are allowed to come freely in contact with the nozzle walls. In such a setup, the virtual mass force associated with the displacement of fluid directly adjacent to the liquid droplet is also neglected due to the much lower density of the vapour.

A.3. Dispersed zero equation model

The turbulence in the continuous phase is modelled with the $k - \omega$ SST model. A dispersed phase zero equation model is applied to evaluate the eddy viscosity of the dispersed phase [61]:

$$\mu_{t,L} = \frac{\rho_L}{\rho_V} \frac{\mu_{t,V}}{P_t} \quad (27)$$

The eddy viscosity of the continuous phase $\mu_{t,V}$ is correlated with the eddy viscosity of the dispersed phase $\mu_{t,L}$ through turbulent Prandtl number P_t, which by default is set to unity. This assumption is suitable as long as the particle relaxation time is short compared to turbulent dissipation time scales [61]. The relaxation time is simply the time required for the dispersed droplets to adjust their velocity to changing flow conditions within the nozzle. Short relaxation times are typical of two-phase flows where the dispersed phase has a smaller density than the continuous phase. In the examined case, the dispersed phase is in the form of liquid droplets, which are expected to have a density at least an order of magnitude higher than the surrounding vapour. In such a case, values higher than unity may need to be used for the turbulent Prandtl number. As an initial assumption, P_t was set to unity.

Appendix B. Validation study

In order to validate the two-fluid model setup, it was applied to simulate flashing of subcooled water in a so-called BNL nozzle [40]. The BNL nozzle is a circular symmetric converging–diverging nozzle, 0.609 m long, with an inlet and outlet diameter of 0.051 m and throat of 0.025 m. The experimental campaign involved a number of experimental runs with different boundary conditions. One particular set-up referred, to as BNL309, will be used for validation purposes, which involved flashing of sub-cooled water at the temperature of 149.1 °C and pressure of 555.9 kPa to the outlet pressure of 402.5 kPa.

Model adjustment

Several amendments had to be made to adjust the two-fluid model described in Section 3 to simulate flash boiling of subcooled water. The dispersed phase was set to be in the form of vapour bubbles, while water liquid was set to be the continuous phase. Wall lubrication force, deemed inapplicable in the case of the wet-to-dry expansion, was included, using a correlation proposed by Hosokawa et al. [70]. Vapour temperature was fixed to the saturation temperature, while the heat-transfer coefficient on the continuous side was evaluated with the Ranz-Marshall correlation [56]. The rest of the set-up remained

Table 4
BNL nozzle: mesh independence study results.

Element count				y_l^+	y_v^+	$\dot{m}_{out}$ [kg/s]	α_v	Mass imbalance [%]
Radial	Circumferential	Axial	Total					
15	40	154	77×10^3	60.1	5.70	8.333	0.744	0.63
23	56	154	168×10^3	63.9	5.88	8.364	0.743	0.79
26	64	192	270×10^3	57.6	5.50	8.369	0.742	0.67
31	72	204	389×10^3	40.9	4.05	8.373	0.741	0.61
32	80	244	527×10^3	41.5	4.22	8.373	0.742	0.70

unchanged. A constant bubble density number of $N_b = 5 \times 10^9$ was assumed in previous studies [44,51], and was also applied in the current simulation. Overall, the setup is similar to these previous studies except for the evaluation of water properties. Both previous studies used the water/steam properties, IAPWS-IF97 [71], which are based on the Helmholtz equation of state [72] and computed directly by the solver. In the current simulation, properties are evaluated by means of look-up tables generated externally using REFPROP 10.0 [62]. The simulation was a 3D steady-state viscous completed in ANSYS CFX 2021 R1 [60].

Mesh independency study

To perform the mesh independence study, several grids were constructed, starting with a coarse 77×10^3-element mesh up to a fine 527×10^3-element grid. Each mesh was a structured mesh constructed with hexahedral elements and was refined in the proximity of the wall and the throat. For every mesh, a converged solution was achieved with mass and momentum residuals below $1e^{-4}$. The results of the mesh independence study are summarised in Table 4. Based on the mesh independence study results, the mesh with 389,000 elements was selected for the validation study.

References

[1] E. Macchi, Theoretical basis of the organic rankine cycle, in: E. Macchi, M. Astolfi (Eds.), Organic Rankine Cycle (ORC) Power Systems, Woodhead Publishing, 2017, pp. 3–24, http://dx.doi.org/10.1016/B978-0-08-100510-1.00001-6.

[2] C. Forman, I.K. Muritala, R. Pardemann, B. Meyer, Estimating the global waste heat potential, Renew. Sustain. Energy Rev. 57 (2016) 1568–1579, http://dx.doi.org/10.1016/j.rser.2015.12.192.

[3] M.D. Albert, K.O. Bennett, C.A. Adams, J.G. Gluyas, Waste heat mapping: A UK study, Renew. Sustain. Energy Rev. 160 (2022) 112230, http://dx.doi.org/10.1016/j.rser.2022.112230.

[4] C. Wieland, F. Dawo, C. Schifflechner, M. Astolfi, Market report on organic rankine cycle power systems: Recent developments and outlook, in: 6th International Seminar on ORC Power Systems, Munich, Germany, 2021, http://dx.doi.org/10.14459/2021mp1636584.

[5] M.G. Read, I.K. Smith, N. Stosic, Multi-variable optimisation of wet vapour organic rankine cycles with twin-screw expanders, in: Proceedings of the 22nd International Compressor Engineering Conference, Purdue, USA, 2014.

[6] J. Chen, X. Zheng, G. Guo, X. Luo, Y. Chen, Z. Yang, A flexible and multifunctional organic rankine cycle system: Preliminary experimental study and advanced exergy analysis, Energy Convers. Manage. 187 (2019) 339–355, http://dx.doi.org/10.1016/j.enconman.2019.03.050.

[7] S.Y. Dibazar, G. Salehi, A. Davarpanah, Comparison of exergy and advanced exergy analysis in three different organic rankine cycles, Processes 8 (5) (2020) 586, http://dx.doi.org/10.3390/pr8050586.

[8] M.T. White, Cycle and turbine optimisation for an ORC operating with two-phase expansion, Appl. Therm. Eng. 192 (2021) 116852, http://dx.doi.org/10.1016/j.applthermaleng.2021.116852.

[9] I.K. Smith, Development of the trilateral flash cycle system: Part 1: Fundamental considerations, Proc. Inst. Mech. Eng. A: J. Power Energy 207 (3) (1993) 179–194, http://dx.doi.org/10.1243/PIME_PROC_1993_207_032_02.

[10] J. Fischer, Comparison of trilateral cycles and organic Rankine cycles, Energy 36 (10) (2011) 6208–6219, http://dx.doi.org/10.1016/j.energy.2011.07.041.

[11] K.Y. Lai, Y.T. Lee, M.R. Chen, Y.H. Liu, Comparison of the trilateral flash cycle and Rankine cycle with organic fluid using the pinch point temperature, Entropy 21 (12) (2019) 1197, http://dx.doi.org/10.3390/e21121197.

[12] M.A. Iqbal, S. Rana, M. Ahmadi, A. Date, A. Akbarzadeh, Trilateral flash cycle (TFC): a promising thermodynamic cycle for low grade heat to power generation, Energy Procedia 160 (2019) 208–214, http://dx.doi.org/10.1016/j.egypro.2019.02.138, 2nd International Conference on Energy and Power, ICEP2018, 13–15 December 2018, Sydney, Australia.

[13] S. Lecompte, H. Huisseune, M. van den Broek, M. De Paepe, Methodical thermodynamic analysis and regression models of organic rankine cycle architectures for waste heat recovery, Energy 87 (2015) 60–76, http://dx.doi.org/10.1016/j.energy.2015.04.094.

[14] Y. Zhou, F. Zhang, L. Yu, Performance analysis of the partial evaporating organic Rankine cycle (PEORC) using zeotropic mixtures, Energy Convers. Manage. 129 (2016) 89–99, http://dx.doi.org/10.1016/j.enconman.2016.10.009.

[15] F. Dawo, J. Buhr, C. Wieland, H. Spliethoff, Experimental investigation of the partially evaporated organic rankine cycle for various heat source conditions, in: 6th International Seminar on ORC Power Systems, Munich, Germany, 2021, http://dx.doi.org/10.14459/2021mp1633102.

[16] I.K. Smith, N. Stošić, C.A. Aldis, Development of the trilateral flash cycle system. Part 3: The design of high-efficiency two-phase screw expanders, Proc. Inst. Mech. Eng. A: J. Power Energy 210 (1) (1996) 75–92, http://dx.doi.org/10.1243/PIME_PROC_1996_210_010_02.

[17] I.K. Smith, N. Stosic, A. Kovacevic, Power recovery from low cost two-phase expanders, Trans. Geotherm. Resour. Counc. (2001) 601–605.

[18] I. Smith, N. Stosic, A. Kovacevic, Screw expanders increase output and decrease the cost of geothermal binary power plant systems, Trans. Geotherm. Resour. Counc. 29 (2005) 787–794.

[19] A.A. Murthy, A. Subiantoro, S. Norris, M. Fukuta, A review on expanders and their performance in vapour compression refrigeration systems, Int. J. Refrig. 106 (2019) 427–446, http://dx.doi.org/10.1016/j.ijrefrig.2019.06.019.

[20] O. Dumont, R. Dickes, V. Lemort, Experimental investigation of four volumetric expanders, Energy Procedia 129 (2017) 859–866, http://dx.doi.org/10.1016/j.egypro.2017.09.206, IV International Seminar on ORC Power Systems, ORC2017 13-15 September 2017, Milano, Italy.

[21] D.G. Elliott, Theory and Tests of Two-Phase Turbines, Jet Propulsion Laboratory, Institute of Technology Pasadena, California, 1982.

[22] L. Hays, J.J. Brasz, A transcritical CO2 turbine-compressor, in: International Compressor Engineering Conference, Paper 1628, 2004, URL https://docs.lib.purdue.edu/icec/1628.

[23] T. He, C. Xia, Y. Zhao, L. Li, P. Shu, An experimental study on energy recovery by a pelton-type expander in a domestic refrigeration system, HVACR Res. 15 (4) (2009) 785–799, http://dx.doi.org/10.1080/10789669.2009.10390864.

[24] M.A. Iqbal, S. Rana, M. Ahmadi, A. Date, A. Akbarzadeh, Experimental study on the prospect of low-temperature heat to power generation using trilateral flash cycle (TFC), Appl. Therm. Eng. 172 (2020) 115139, http://dx.doi.org/10.1016/j.applthermaleng.2020.115139.

[25] H. Li, S. Rane, Z. Yu, G. Yu, An inverse mean-line design method for optimizing radial outflow two-phase turbines in geothermal systems, Renew. Energy 168 (2021) 463–490, http://dx.doi.org/10.1016/j.renene.2020.12.079.

[26] S. Rane, L. He, Numerical analysis of a novel two-phase turbine using thermal non-equilibrium, homogeneous nucleation phase change, Therm. Sci. Eng. Prog. 22 (2021) 100827, http://dx.doi.org/10.1016/j.tsep.2020.100827.

[27] A. Date, A. Khaghani, J. Andrews, A. Akbarzadeh, Performance of a rotating two-phase turbine for combined power generation and desalination, Appl. Therm. Eng. 76 (2015) 9–17, http://dx.doi.org/10.1016/j.applthermaleng.2014.08.074.

[28] A. Date, S. Vahaji, J. Andrews, A. Akbarzadeh, Experimental performance of a rotating two-phase reaction turbine, Appl. Therm. Eng. 76 (2015) 475–483, http://dx.doi.org/10.1016/j.applthermaleng.2014.11.039.

[29] A. Renuke, A. Vannoni, M. Pascenti, A. Traverso, Experimental and numerical investigation of small-scale tesla turbines, J. Eng. Gas Turbines Power 141 (12) (2019) 1–14, http://dx.doi.org/10.1115/1.4044999.

[30] L. Talluri, O. Dumont, G. Manfrida, V. Lemort, D. Fiaschi, Experimental investigation of an organic rankine cycle tesla turbine working with R1233zd(e), Appl. Therm. Eng. 174 (2020) 115293, http://dx.doi.org/10.1016/j.applthermaleng.2020.115293.

[31] E. Ortego Sampedro, L. Védie, Diphenyl-diphenyl oxide eutectic mixture for high temperature waste-heat valorization by a partially evaporated cycle cascade, Energy 263 (2023) 125812, http://dx.doi.org/10.1016/j.energy.2022.125812.

[32] M.T. White, Investigating the wet-to-dry expansion of organic fluids for power generation, Int. J. Heat Mass Transfer 192 (2022) 122921, http://dx.doi.org/10.1016/j.ijheatmasstransfer.2022.122921.

[33] G. Lhermet, N. Tauveron, N. Caney, Q. Blondel, F. Morin, A recent advance on partial evaporating organic rankine cycle: Experimental results on an axial turbine, Energies 15 (20) (2022) 7559, http://dx.doi.org/10.3390/en15207559.

[34] Y. Liao, D. Lucas, Computational modelling of flash boiling flows: A literature survey, Int. J. Heat Mass Transfer 111 (2017) 246–265, http://dx.doi.org/10.1016/j.ijheatmasstransfer.2017.03.121.

[35] Y. Liao, D. Lucas, A review on numerical modelling of flashing flow with application to nuclear safety analysis, Appl. Therm. Eng. 182 (2021) 116002, http://dx.doi.org/10.1016/j.applthermaleng.2020.116002.

[36] S. Leyer, M. Wich, The integral test facility karlstein, Sci. Technol. Nucl. Install. 2012 (2011) 439374, http://dx.doi.org/10.1155/2012/439374.

[37] Y. Liao, D. Lucas, Possibilities and limitations of CFD simulation for flashing flow scenarios in nuclear applications, Energies 10 (1) (2017) http://dx.doi.org/10.3390/en10010139.

[38] D. Sallet, Critical mass flow rates through pressure relief valves, Wärme-Stoffübertrag. 26 (6) (1991) 315–321, http://dx.doi.org/10.1007/BF01591664.

[39] R.E. Henry, H.K. Fauske, The two-phase critical flow of one-component mixtures in nozzles, orifices, and short tubes, J. Heat Transfer 93 (2) (1971) 179–187, http://dx.doi.org/10.1115/1.3449782.

[40] N. Abuaf, B.J. Wu, G.A. Zimmer, P. Saha, Study of Nonequilibrium Flashing of Water in a Converging-Diverging Nozzle. Volume 1: Experimental, Brookhaven National Laboratory, 1981.

[41] M. Haida, J. Smolka, A. Hafner, M. Palacz, K. Banasiak, A.J. Nowak, Modified homogeneous relaxation model for the R744 trans-critical flow in a two-phase ejector, Int. J. Refrig. 85 (2018) 314–333, http://dx.doi.org/10.1016/j.ijrefrig.2017.10.010.

[42] L. Geng, H. Liu, X. Wei, CFD analysis of the flashing flow characteristics of subcritical refrigerant R134a through converging-diverging nozzles, Int. J. Therm. Sci. 137 (2019) 438–445, http://dx.doi.org/10.1016/j.ijthermalsci.2018.12.011.

[43] M. Loska, J. Smolka, M. Haida, E.E. Kriezi, K. Banasiak, CFD modelling of R410A flow through an expansion valve using equilibrium and modified relaxation models, Appl. Therm. Eng. 185 (2021) 116442, http://dx.doi.org/10.1016/J.APPLTHERMALENG.2020.116442.

[44] S. Rane, L. He, CFD analysis of flashing flow in two-phase geothermal turbine design, J. Comput. Des. Eng. 7 (2) (2020) 238–250, http://dx.doi.org/10.1093/jcde/qwaa020.

[45] P. Downar-Zapolski, Z. Bilicki, L. Bolle, J. Franco, The non-equilibrium relaxation model for one-dimensional flashing liquid flow, Int. J. Multiph. Flow. 22 (3) (1996) 473–483, http://dx.doi.org/10.1016/0301-9322(95)00078-X.

[46] D.P. Schmidt, S. Gopalakrishnan, H. Jasak, Multi-dimensional simulation of thermal non-equilibrium channel flow, Int. J. Multiph. Flow. 36 (4) (2010) 284–292, http://dx.doi.org/10.1016/j.ijmultiphaseflow.2009.11.012.

[47] S. Mimouni, M. Boucker, J. Laviéville, A. Guelfi, D. Bestion, Modelling and computation of cavitation and boiling bubbly flows with the NEPTUNE_CFD code, Nucl. Eng. Des. 238 (3) (2008) 680–692, http://dx.doi.org/10.1016/j.nucengdes.2007.02.052.

[48] M. Robert, M. Farvacque, M. Parent, B. Faydide, CATHARE 2 V2.5 : a fully validated CATHARE version for various applications, in: Proceedings of the 10th International Topical Meeting on Nuclear Reactor Thermal-Hydraulics (NURETH 10), Seoul, Korea, 2003.

[49] C. Marsh, A. O'Mahony, Three-dimensional modelling of industrial flashing flows, Prog. Comput. Fluid Dyn. Int. J. 9 (6/7) (2009) 393, http://dx.doi.org/10.1504/PCFD.2009.027370.

[50] J.P. Janet, Y. Liao, D. Lucas, Heterogeneous nucleation in CFD simulation of flashing flows in converging-diverging nozzles, Int. J. Multiph. Flow. 74 (2015) 106–117.

[51] Y. Liao, D. Lucas, 3D CFD simulation of flashing flows in a converging-diverging nozzle, Nucl. Eng. Des. 292 (2015) 149–163, http://dx.doi.org/10.1016/j.nucengdes.2015.06.015.

[52] A. Edwards, T. O'Brian, Studies of phenomena connected with the depressurization of water reactors, J. Br. Nucl. Enery Soc. 9 (2) (1970) 125–135.

[53] A. Schaffrath, A.-K. Krüssenberg, F.-P. Weiss, E. Hicken, M. Beyer, H. Carl, H.-M. Prasser, J. Schuster, P. Schütz, M. Tamme, W. Zimmermann, TOPFLOW - A new multipurpose thermalhydraulic test facility for the investigation of steady state and transient two phase flow phenomena, Kerntechnik 66 (2001) 209–213, http://dx.doi.org/10.1515/kern-2001-0086.

[54] E. Ortego Sampedro, F. Breque, M. Nemer, Two-phase nozzles performances CFD modeling for low-grade heat to power generation: mass transfer models assessment and a novel transitional formulation, Therm. Sci. Eng. Prog. (2021) 101139.

[55] E. Laurien, Influence of the model bubble diameter on three-dimensional numerical simulations of thermal cavitation in pipe elbows, in: Proceedings of the 3rd International Symposium on Two-Phase Flow Modelling and Experimentation, Pisa, Italy, 2004.

[56] W.E. Ranz, W.R. Marshall Jr., Evaporation from drops: Part 1, Chem. Eng. Prog. 48 (3) (1952) 141–146.

[57] ANSYS Inc., CFX-Solver Modelling Guide, Release 2021 R1.

[58] M. Ishii, N. Zuber, Drag coefficient and relative velocity in bubbly, droplet or particulate flows, AIChE J. 25 (5) (1979) 843–855.

[59] A. Tomiyama, Struggle with computational bubble dynamics, in: Proceedings of Third International Conference on Multiphase Flow, Lyon, France, 1998.

[60] ANSYS Inc., ANSYS CFX, Release 2021 R1.

[61] ANSYS Inc., CFX-Solver Theory Guide, Release 2021 R1.

[62] E.W. Lemmon, I.H. Bell, M.L. Huber, M.O. McLinden, NIST Standard Reference Database 23: Reference Fluid Thermodynamic and Transport Properties-REFPROP, Version 10.0, National Institute of Standards and Technology, 2018, https://www.nist.gov/srd/refprop.

[63] M. Thol, F. Dubberke, G. Rutkai, T. Windmann, A. Köster, R. Span, J. Vrabec, Fundamental equation of state correlation for hexamethyldisiloxane based on experimental and molecular simulation data, Fluid Phase Equilib. 418 (2016) 133–151, http://dx.doi.org/10.1016/j.fluid.2015.09.047.

[64] J.R. Grace, T. Wairegi, T.H. Nguyen, Shapes and velocities of single drops and bubbles moving freely through immiscible liquids, Trans Instit. Chem. Eng. (3) (1976) 167–173.

[65] L. Schiller, A. Naumann, A drag coefficient correlation, Vdi Zeitung 77 (1935) 318–320.

[66] K. Wolfert, The simulation of blowdown processes with consideration of thermodynamic nonequilibrium phenomena, in: Proceedings of the Specialists Meeting of Transient Two-Phase Flow, OECD/Nuclear Energy Agency, Toronto, ON, Canada, 1976.

[67] D.R. Guildenbecher, C. López-Rivera, P.E. Sojka, Secondary atomization, Exp. Fluids 46 (3) (2009) 371–402, http://dx.doi.org/10.1007/s00348-008-0593-2.

[68] R. Brodkey, Formation of drops and bubbles, in: The Phenomena of Fluid Motions, Addison-Wesley, Reading, 1967.

[69] V.E. Nakoryakov, Study of upward bubbly flow at low liquid velocities, Izv. sib. Otdel Akad. Nauk SSSR 16 (1986) 15–20.

[70] S. Hosokawa, A. Tomiyama, S. Misaki, T. Hamada, Lateral migration of single bubbles due to the presence of wall, in: Proceedings of the ASME 2002 Joint U.S.-European Fluids Engineering Division Conference. Volume 1: Fora, Parts a and B, pp. 855–860, http://dx.doi.org/10.1115/FEDSM2002-31148, Montreal, Quebec, Canada. July 14–18, 2002. pp.855-860.

[71] The International Association for the Properties of Water and Steam, Revised release on the IAPWS industrial formulation 1997 for the thermodynamic properties of water and steam, 2018, http://www.iapws.org/relguide/IF97-Rev.html.

[72] E.W. Lemmon, R. Tillner-Roth, A Helmholtz energy equation of state for calculating the thermodynamic properties of fluid mixtures, Fluid Phase Equilib. 165 (1) (1999) 1–21, http://dx.doi.org/10.1016/S0378-3812(99)00262-9.